Radial shear in the flow at the Earth's core surface

I Firsov, Dominique Jault, N Gillet, J Aubert, M Mandea

submitted to *Geophys. J. Int.*

Radial shear in the flow at the Earth's core surface

I. Firsov[1,3], D. Jault[1], N. Gillet[1], J. Aubert[2] and M. Mandea[3],

[1] *Univ. Grenoble Alpes, Univ. Savoie Mont Blanc, CNRS, IRD, UGE, ISTerre, 38000 Grenoble, France*

[2] *Univ. Paris Cité, Institut de Physique du Globe de Paris, CNRS, 75005 Paris, France*

3 *CNES – Centre National d'Etudes Spatiales, 2 place Maurice Quentin, 75039 Paris Cedex 01, France*

15 September 2023

SUMMARY

The Earth's magnetic field at the core-mantle boundary is the gradient of a harmonic potential function if the mantle is electrically insulating, and the horizontal components of the field can be derived from its radial component in the mantle. Therefore, these components give no further observational information on the core dynamics. However, it can still be envisioned that the horizontal components of the induction equation at Earth's core surface yield further knowledge on the fluid motions at the top of the core independently of the observations. Here, we show that they provide a linear relationship between the surface velocity and the surface shear (strain shear) that depends on the mantle electrical conductivity. This offers a protocol to calculate the surface shear that we validate with synthetics obtained from dynamo simulations in the limit of a weak mantle conductance. Firstly, using numerical simulations with stress-free boundary condition at the core surface, we retrieve the expected relationship between the horizontal flow $\mathbf{u}_\Sigma$ and the shear, $\mathbf{u}_\Sigma = r\partial_r \mathbf{u}_\Sigma$. Next, we investigate simulations with no-slip boundary condition and insulating mantle, and we obtain the same relationship, even though the shear is not imposed as a boundary condition. Finally, we calculate the flow shear at the top of the core from a magnetic field model based on satellite measurements. The application to geophysical data indicates larger values of the surface flow shear than in the synthetic case, suggesting a possible role of the mantle electrical conductivity. The surface flow shear, in

the simulations, much differs from the radial shear in the flow, deeper in the core, which is influenced by the mostly quasi-geostrophic geometry. This implies that we cannot rely on the relationship between the flow and the radial shear for quasi-geostrophic motions to exploit the horizontal components of the induction equation and gain further information on the flow at the Earth's core surface.

key words: Core; Magnetic field variations through time; Inverse theory.

1 INTRODUCTION

The Earth's magnetic field has been recorded from low Earth's orbiting satellites for most of the time since 1999 and from ground observatories since the first half of the 19th century. Models describing the Earth's main magnetic field $\mathbf{B}$ and its temporal variations can be built at the planet's surface (of radius $r = r_E$). They can be continued to the core-mantle boundary (CMB, $r = r_C$) if the mantle is treated as an electrical insulator, since $\mathbf{B}$ can be written as the gradient of a harmonic function for $r_C \leq r \leq r_E$. There is a host of analyses, based on the diffusion-free radial induction equation, of the large scale part of the core surface flow $\mathbf{u}_\Sigma$ from the time changes of the radial component B_r of $\mathbf{B}$ (e.g. Jackson and Bloxham 1991; Eymin and Hulot 2005; Pais and Jault 2008; Bärenzung et al. 2018; Gillet et al. 2019). Because $\mathbf{B}$ at the CMB is the gradient of a harmonic function if the mantle is insulating, the horizontal components $\mathbf{B}_H$ of $\mathbf{B}$ can be derived from its radial component B_r in the mantle. Therefore, these components do not give further observational information on the core dynamics, additionally to the radial field (Jault and Le Mouël 1991). In other terms, the radial induction equation suffices to extract all the available information from the magnetic field temporal changes at the CMB.

However, it can still be envisioned that the horizontal components of the induction equation yield further knowledge on the flow next to the core surface independently of the observations. Actually, additional information on the flow at the top of the core from the tangential components of the induction equation is conditional to analyses of the hydromagnetic layer at the CMB. A thin diffusive layer can be modelled as a current sheet. Located at the boundary of a perfectly conducting fluid, it corresponds to a jump in the tangential components of the magnetic field

between the top of the free stream below the diffusive boundary layer and the surface. A series of studies have concluded that the tangential field discontinuity is small compared to the field itself. First, in a non-rotating and inviscid case, Stewartson (1957) argued that any current sheet in the presence of a transverse magnetic field would immediately spawn Alfvén waves that eliminate the discontinuity in the tangential magnetic field. Stewartson (1960) found that this conclusion holds also for viscous hydromagnetic layers provided that the magnetic Prandtl number $P_m = \nu/\eta$ is small enough, $P_m \ll 1$ (ν the kinematic viscosity, η the magnetic diffusivity), which is the case for liquid metals. Roberts and Scott (1965) reckoned in their analysis of the SV that this result applies to the boundary layer at the core surface. Finally, Hide and Stewartson (1972) investigated the viscous boundary layer associated with hydromagnetic oscillations of the Earth's core. They accounted for the Coriolis term in the boundary layer equations and found again the discontinuity in $\mathbf{B}_H$ to be negligible.

The scenario first set out by Stewartson (1957) does not work if the fluid cannot sustain hydromagnetic waves able to disperse the discontinuity in the magnetic field. This happens when flows are restricted to a narrow class such as rigid rotations or geostrophic motions. As a first example, Loper and Benton (1970) investigated the spin-up of an electrically conducting fluid and found that the viscous Ekman-Hartmann layer is embedded in a thicker continuously growing magnetic diffusion layer. Similarly, Braginsky (1970) and Roberts and Soward (1972) considered a diffusive layer encompassing the Ekman layer in their study of torsional Alfvén waves, which consist of geostrophic motions. We can wonder whether this approach extends to less constrained flows such as Quasi-Geostrophic (QG) motions. Jault and Le Mouël (1991) investigated a magnetic field varying with time as $\exp(-2\mathrm{i}\pi t/\tau)$ in the Earth's core and the associated diffusive layer. Taking τ as 10 years, they concluded that the Lorentz force arising from the electrical currents in the diffusive layer is negligible in comparison with the Coriolis force. They found, therefore, that it cannot disrupt the diffusive layer in contrast with the scenario set out by Stewartson (1957). From this point, studies of core surface flow have been based on the radial component of the induction equation only.

Recent numerical geodynamo simulations, calculated with no-slip boundary conditions, do not

clearly show a magnetic diffusion layer encompassing the viscous Ekman layer. Indications of a significant contribution of the Lorentz force in the boundary layer attached to the CMB can be found in Fig. 18 by Schaeffer et al. (2017) and Fig. 5 by Schwaiger et al. (2019) – see their most viscous case. This points to the presence of electrical currents that may cause a discontinuity of the magnetic field components tangent to the core surface across the boundary layer. However, this effect might be negligible for geophysical realistic viscosities.

The boundary condition on the magnetic field involved in the propagation in the Earth's core of one-dimensional torsional Alfvén waves $u_G(s)\mathbf{e}_\phi$ (where (s, ϕ, z) are cylindrical coordinates and $\mathbf{e}_\phi$ the unit vector in the ϕ direction) governs their reflection at $s = r_C$. As for generic Alfvén waves, there is only one boundary condition involving both the flow and the magnetic field at the interface with the solid mantle (Schaeffer and Jault 2016). When the mantle is an insulator (and $P_m \ll 1$), the appropriate condition at $s = r_C$ is $B_\phi = 0$ (*i.e.* continuity with the zero zonal toroidal field in the mantle). Jackson and Maffei (2020) extended the approach to a two-dimensional model and assumed the continuity of the three components of the magnetic field at the CMB to calculate the surface terms for the magnetic force in their QG model of core dynamics, where magnetic diffusion is neglected. Finally, Gerick et al. (2021) calculated QG hydromagnetic oscillations and Luo et al. (2022) more general waves imposing that the magnetic field perturbation matches a potential field at the boundary with the insulating mantle.

If there is no or negligible discontinuity of the tangential field across a diffusive boundary layer, the horizontal components of the induction equation give two independent and complementary constraints that the flow has to satisfy for the magnetic field at the top of the core to match a potential field in the mantle. The two constraints involve the two horizontal components of the surface shear $r\partial \mathbf{u}_\Sigma/\partial r$ (Lloyd and Gubbins 1990; Jackson and Bloxham 1991). They can be expressed as a relationship between $r\partial \mathbf{u}_\Sigma/\partial r$ and $\mathbf{u}_\Sigma$ at the core surface, function of the radial field B_r. In order to go further, we can examine how the flow and the radial shear are related in Earth-like geodynamo simulations. The goal is to develop a protocol to describe as well as possible the outer core dynamics from geomagnetic models.

We derive in §2 the relationship between the surface flow and shear obtained after matching

the SV at the core surface with a potential field in the mantle. We show also how this relationship is modified in the presence of a thin conducting layer in the mantle that affects the horizontal components of the SV, but not its radial component. Next, we present in §3 the magnetic data (synthetic data from dynamo simulations and geomagnetic field models) used for our study. Inversion of the surface flow from SV models and of the surface shear from flow models involve prior information provided as covariance matrices for $\mathbf{u}_\Sigma$, $r\partial\mathbf{u}_\Sigma/\partial r$ and the error terms. A description of these matrices is given in §4 together with the set-up for solving the inverse problem. Validation from synthetic data and models of the surface shear from geomagnetic data are presented in section §5. The paper ends with a discussion.

2 EQUATIONS FOR THE RADIAL SHEAR IN THE FLOW AT THE CORE SURFACE

2.1 Condition on induction at the core surface

We first assume the mantle to be electrically insulating. Then, the magnetic field can be written in the mantle as

$$\mathbf{B} = -\boldsymbol{\nabla}\Phi, \tag{1}$$

with the magnetic potential

$$\Phi = \sum_{l=1}^{\infty}\sum_{m=-l}^{l} \Phi_l^m \left(\frac{r_C}{r}\right)^{l+1} Y_l^m(\theta,\phi), \tag{2}$$

(r,θ,ϕ) spherical coordinates, and l and m spherical harmonic degree and order. We consider the spherical harmonics Y_l^m to be fully normalized:

$$\int Y_l^m (Y_{l'}^{m'})^\dagger \sin\theta \mathrm{d}\theta\mathrm{d}\phi = 4\pi\delta_l^{l'}\delta_m^{m'}. \tag{3}$$

The condition

$$\Phi_l^{-m} = (-1)^m(\Phi_l^m)^\dagger \tag{4}$$

ensures that the scalar field Φ is real. In the core, we use the scaloidal/poloidal/toroidal (Helmoltz) representation of a vector field (Backus et al. 1996; Ivers and Phillips 2008), which is valid for any

vector field

$$\begin{aligned}
&\mathbf{B} = U_B(r,\theta,\phi)\mathbf{e}_r + \boldsymbol{\nabla}_1 V_B(r,\theta,\phi) + \mathbf{e}_r \times \boldsymbol{\nabla}_1 W_B(r,\theta,\phi),\\
\text{with}\quad &U_B = \sum_{l=0}^{l=\infty}\sum_{m=-l}^{l} U^m_{B,l}(r) Y^m_l(\theta,\phi), \quad V_B = \sum_{l=1}^{l=\infty}\sum_{m=-l}^{l} V^m_{B,l}(r) Y^m_l(\theta,\phi),\\
&W_B = \sum_{l=1}^{l=\infty}\sum_{m=-l}^{l} W^m_{B,l}(r) Y^m_l(\theta,\phi),
\end{aligned} \tag{5}$$

and $\boldsymbol{\nabla}_1 V = (r\boldsymbol{\nabla} - r\partial/\partial r)V$. The condition that $\mathbf{B}$ is solenoidal yields

$$V^m_{B,l} = \frac{1}{r}\frac{1}{l(l+1)}\frac{\partial}{\partial r}(r^2 U^m_{B,l}). \tag{6}$$

At the CMB, $\mathbf{B}$ has to match with a potential field of the form (1). The continuity of $\mathbf{B}$ at $r = r_C$ implies the continuity of U_B, V_B, W_B and, as a consequence of (6), the continuity of $\partial U_B/\partial r$. The toroidal component vanishes:

$$W^m_{B,l}(c) = 0. \tag{7}$$

At $r = r_C$, we have $V_B = -\phi/r$ and $U_B = -\partial\phi/\partial r$. As a result, the poloidal coefficients satisfy the relationship (see (6))

$$U^m_{B,l} = -(l+1)V^m_{B,l} = -\frac{1}{rl}\frac{\partial(r^2 U^m_{B,l})}{\partial r}. \tag{8}$$

The same conditions hold for the secular variation field $\partial\mathbf{B}/\partial t$ and for the vector field $\boldsymbol{\nabla} \times (\mathbf{u} \times \mathbf{B})$ if the magnetic field satisfies the diffusionless induction equation at $r = r_C$,

$$\frac{\partial \mathbf{B}}{\partial t} = \boldsymbol{\nabla} \times (\mathbf{u} \times \mathbf{B}). \tag{9}$$

We introduce different notations for the velocity $\mathbf{u}$ and its surface expression $\mathbf{u}_\Sigma$ because $\partial u_r/\partial r \neq 0$. Consequently, $\partial \mathbf{u}_\Sigma/\partial r \neq \partial \mathbf{u}/\partial r$ although $\mathbf{u}_\Sigma = \mathbf{u}$ at $r = r_C$.

We can also use the Helmoltz representation, which does not require the vector field to be divergence-less, for $\mathbf{v} = \mathbf{u} \times \mathbf{B}$,

$$\mathbf{v} = U(r,\theta,\phi)\mathbf{e}_r + \boldsymbol{\nabla}_1 V(r,\theta,\phi) + \mathbf{e}_r \times \boldsymbol{\nabla}_1 W(r,\theta,\phi). \tag{10}$$

This can be transformed into

$$B_r \mathbf{u}_\Sigma = -\boldsymbol{\nabla}_1 W + \mathbf{e}_r \times \boldsymbol{\nabla}_1 V, \tag{11}$$

which is analogous to the equation (20) of Backus (1968). We are interested by $\boldsymbol{\nabla} \times (\mathbf{u} \times \mathbf{B})$:

$$\boldsymbol{\nabla} \times \mathbf{v} = -\frac{1}{r} L^2 W \mathbf{e}_r - \frac{1}{r} \boldsymbol{\nabla}_1 \left(\frac{\partial (rW)}{\partial r} \right) - \frac{1}{r} \mathbf{e}_r \times \boldsymbol{\nabla}_1 \left(U - \frac{\partial (rV)}{\partial r} \right), \tag{12}$$

where

$$L^2 (W_l^m Y_l^m(\theta, \phi)) = l(l+1) W_l^m Y_l^m(\theta, \phi). \tag{13}$$

Therefore, the radial induction equation becomes

$$\forall l, m, \qquad \frac{\partial U_{B,l}^m}{\partial t} = -\frac{l(l+1)}{r} W_l^m. \tag{14}$$

This equation enables us to estimate the surface velocity $\mathbf{u}_\Sigma$ from the radial SV. It corresponds, for example, to the expression (21) of Backus (1968).

In addition, two conditions on the toroidal and poloidal components of the vector field $\boldsymbol{\nabla} \times (\mathbf{u} \times \mathbf{B})$ ensure that $\partial \mathbf{B} / \partial t$ matches a potential field. These conditions do not directly involve the SV observations. The condition on the toroidal part of $\boldsymbol{\nabla} \times (\mathbf{u} \times \mathbf{B})$ yields

$$U = \frac{\partial (rV)}{\partial r}. \tag{15}$$

Combining (8) and (12), the condition on the poloidal part is satisfied when

$$\forall l, m, \qquad \frac{\partial (r W_l^m)}{\partial r} = -l W_l^m. \tag{16}$$

From (11), we find that the complementary conditions (15) and (16) relate the surface flow and its radial derivative. In the following, we proceed by first calculating the surface flow $\mathbf{u}_\Sigma$ from the radial SV. Second, we rely on the conditions (15) and (16) to estimate $r \partial \mathbf{u}_\Sigma / \partial r$ from our model for $\mathbf{u}_\Sigma$. Our approach can be summarized as the sequential solution of the following set of equations at $r = r_C$:

$$\frac{\partial B_r}{\partial t} = -\frac{1}{r_C} \boldsymbol{\nabla}_1 \cdot (\mathbf{u}_\Sigma B_r), \tag{17}$$

$$A_u(B_r) \mathbf{u}_\Sigma = A_\delta(B_r) \left(r \frac{\partial \mathbf{u}_\Sigma}{\partial r} \right). \tag{18}$$

where A_u and A_δ are linear operators.

2.2 Influence of a conducting layer at the base of the mantle

Now, we discuss how the conditions (15) and (16) are modified in the presence of a thin conducting layer at the bottom of the mantle. We distinguish two electromagnetic diffusion times constructed from the electrical conductivity σ_m of the layer: $\tau_G = \mu\sigma_m r_C \delta_m$ and $\tau_F = \mu\sigma_m \delta_m^2$ where δ_m is the thickness of the conducting layer and μ the magnetic permeability. The time τ_F arises in the discussion of induction in the mantle from time-varying core fields. Therefore, we note it τ_F as a reference to Faraday's law of induction. It is also known as the screening time of the mantle. We write the second time τ_G as a reference to galvanic (electrical) contact between the flowing core and the conducting layer in the mantle. The boundary conditions on the magnetic field that we write below are based indeed on the continuity of the electrical field, assuming galvanic contact at the CMB. This mechanism is similar to the galvanic excitation of the conducting upper mantle from M2 tidal currents (Schnepf et al. 2015). The time τ_G can also be described as a magnetic friction time (Braginsky 1984). We assume here $\tau_F \ll \tau_{SV}$, where τ_{SV}/l is a typical time scale of the SV for each spherical harmonic degree l (Lhuillier et al. 2011), while τ_G, conversely, may be of the order of τ_{SV}. The assumption $\tau_F \ll \tau_{SV}$ enables us to take the radial magnetic field as continuous across the layer (Jault 2015): the radial induction equation is unaffected by the inclusion of the conducting layer in the model.

We write in the layer

$$\mathbf{B} = -\boldsymbol{\nabla}\Phi + \mathbf{B}_\delta, \tag{19}$$

where $\mathbf{B}_\delta$ is a horizontal field parallel to the core-mantle boundary. Under the thin layer approximation, the diffusive equation in the conducting layer simplifies as $\partial^2 \mathbf{B}_\delta / \partial r^2 = 0$. As a result, $\mathbf{B}_\delta$ is proportional to the distance to the top of the layer ($r = r_C + \delta_m$), where it vanishes. We finally obtain

$$\mathbf{B} = -\boldsymbol{\nabla}\Phi + \frac{r_C + \delta_m - r}{\delta_m} \mathbf{B}_\delta \mid_{r=r_C}, \tag{20}$$

We expand $\mathbf{B}_\delta$ at the CMB as

$$\mathbf{B}_\delta \mid_{r=r_C} = \boldsymbol{\nabla}_1 V_\delta(r,\theta,\phi) + \mathbf{e}_r \times \boldsymbol{\nabla}_1 W_\delta(r,\theta,\phi). \tag{21}$$

Then, we can write the electrical field at the bottom of the mantle as

$$\mathbf{E} = \frac{\mathbf{j}}{\sigma_m} = \frac{1}{\mu\sigma_m}\left(-\boldsymbol{\nabla}_1\left(\frac{\partial W_\delta}{\partial r}\right) + \mathbf{e}_r \times \boldsymbol{\nabla}_1\left(\frac{\partial V_\delta}{\partial r}\right)\right), \tag{22}$$

where $\mathbf{j}$ is the electrical current density. On the core side of the boundary, we have $\mathbf{E} = -\mathbf{u} \times \mathbf{B}$, because we assume the core to be perfectly conducting, and

$$\frac{\partial W_\delta}{\partial r} = -\mu\sigma_m V, \qquad \frac{\partial V_\delta}{\partial r} = \mu\sigma_m W. \tag{23}$$

We seek to impose that $\boldsymbol{\nabla} \times (\mathbf{u} \times \mathbf{B}) - \partial \mathbf{B}_\delta/\partial t$ matches a potential field at $r = r_C$. The condition of no induction of toroidal field is transformed into

$$\begin{aligned} \frac{1}{r}\left(\frac{\partial (rV)}{\partial r} - U\right) = \frac{\partial W_\delta}{\partial t} = -\delta_m \frac{\partial}{\partial t}\left(\frac{\partial W_\delta}{\partial r}\right) = \delta_m \mu\sigma_m \frac{\partial V}{\partial t}, \\ \frac{\partial (rV)}{\partial r} - U = \tau_G \frac{\partial V}{\partial t}, \end{aligned} \tag{24}$$

and the condition on the poloidal field becomes

$$\forall l, m, \qquad -\frac{1}{r} l(l+1) W_l^m = (l+1)\left(\frac{1}{r}\frac{\partial (rW_l^m)}{\partial r} + \frac{\partial V_{\delta,l}^m}{\partial t}\right) \tag{25}$$

which gives

$$\forall l, m, \qquad \frac{\partial (rW_l^m)}{\partial r} = -lW_l^m + \tau_G \frac{\partial W_l^m}{\partial t}. \tag{26}$$

In order to put the equations 24 and 26 in perspective, we can relate them to the study of Schaeffer and Jault (2016) who considered torsional Alfvén waves with velocity V_A in the cylindrical radial direction. These waves consist of rigid rotations $\mathbf{u}_G(s,t)$ of geostrophic cylinders (where s is the distance to the rotation axis). Inserting $u_G \propto \exp(\mathrm{i}k(V_A t \pm s))$ in equations 24 and 26, we introduce the dimensionless number $Q = \tau_G V_A / r_C$, in front of the term dependent on mantle conductivity. Here, $V_A = |B_r|(r = r_C)/\sqrt{\rho\mu}$ is constructed from the radial magnetic field at the CMB (ρ the outer core density). Schaeffer and Jault (2016) found that this number governs the reflection of torsional waves at $s = r_C$. Assuming Q is $O(1)$ or smaller, mantle conductivity has negligible influence on large-scale flows with time scale $\tau \gg r_C/V_A$ (about 20 years in the Earth's case). The numerical simulations we consider here satisfy this hypothesis (see §3.1).

2.3 Expressions in terms of vector spherical harmonics

We transform the conditions (15) and (16) into relations between the velocity and its radial derivative from vector spherical harmonic expansions of $\mathbf{u}$ and $\mathbf{v} = \mathbf{u} \times \mathbf{B}$ (Phinney and Burridge 1973; Ivers and Phillips 2008). The same formalism has been used before by Jackson and Bloxham (1991) for the poloidal components of the induction equation and by Greff-Lefftz and Legros (1995) in the context of electromagnetic core-mantle coupling. It enables us to replace horizontal derivatives by projections. It involves the complex basis defined as

$$\mathbf{e}_\pm = \frac{1}{\sqrt{2}}(\mp\mathbf{e}_\theta - \mathrm{i}\mathbf{e}_\phi), \quad \mathbf{e}_0 = \mathbf{e}_r. \tag{27}$$

The contravariant components of $\mathbf{v}$ in this basis are

$$v^\pm = \mathbf{v}\cdot\mathbf{e}^\pm = \mathbf{v}\cdot\mathbf{e}_\pm^\dagger = \frac{1}{\sqrt{2}}\left(\mp v^\theta + \mathrm{i}v^\phi\right), \quad v^0 = v^r. \tag{28}$$

The components $v^\pm$ are expanded in generalized spherical harmonics

$$v^\pm = \sum_{l=1}^{l=\infty}\sum_{m=-l}^{l} v_l^{\pm,m} Y_l^{\pm,m}, \tag{29}$$

where

$$Y_l^{\pm,m}(\theta,\phi) = \widehat{P}_l^{N,m}(\mu)\exp(\mathrm{i}m\phi) \tag{30}$$

and $\widehat{P}_l^{N,m}(\mu)$ are generalized and normalized associate Legendre functions. They are real-valued. The generalized surface harmonics obey the same orthogonality relation as the classical ones:

$$\forall N, \qquad \iint Y_l^{N,m}(Y_{l'}^{N,m'})^\dagger \sin\theta \mathrm{d}\theta\mathrm{d}\phi = 4\pi\delta_l^{l'}\delta_m^{m'} \tag{31}$$

(see Appendix A).

The two representations (10) and (28)-(29) of a vector field $\mathbf{v}$ are related through

$$\forall l \geq 1, -l \leq m \leq l, \quad v_l^{\pm,m} = \frac{\sqrt{l(l+1)}}{\sqrt{2}}\left(V_l^m \mp \mathrm{i}W_l^m\right), \quad v_l^{0,m} = U_l^m. \tag{32}$$

We have also

$$v_l^{\pm,m} = (-1)^m (v_l^{\mp,-m})^\dagger, \tag{33}$$

and, in particular,

$$v_l^{+,0} = (v_l^{-,0})^\dagger. \tag{34}$$

Henceforth, we keep the notation $v^{\pm}, v^0$ for the complex basis components of the vector field $\mathbf{v} = \mathbf{u} \times \mathbf{B}$. The components of $\mathbf{u}$ are $u^{\pm}$ and u^0. From identity (32), equation (11) yields

$$v^{\pm} = \pm \mathrm{i} B_r u^{\pm}. \tag{35}$$

Using (32) again, the radial induction (14) can be written as

$$\forall l \geq 1, \forall m \in [0, l], \quad \frac{\partial U^m_{B,l}}{\partial t} = -\mathrm{i} \frac{\sqrt{l(l+1)}}{\sqrt{2} r} \left(v_l^{+,m} - v_l^{-,m} \right). \tag{36}$$

This equation is valid for both positive and negative m but we have to write it only for positive m as the identity for negative m can be obtained from the complex conjugate of the identity for positive m. Combining (35) and (36), we obtain the linear relationship between the flow and SV coefficients.

The condition (15) of no toroidal field induction can be transformed into

$$\forall l \geq 1, \forall m \in [0, l], \quad \sqrt{2l(l+1)} v_l^{0,m} = \frac{\partial}{\partial r} r \left(v_l^{+,m} + v_l^{-,m} \right). \tag{37}$$

We can detail the above relation from the decomposition

$$\frac{\partial}{\partial r} (r \mathbf{v})_{\Sigma} = \mathbf{p} + \mathbf{s} + \mathbf{t}, \tag{38}$$

where the subscript Σ means tangential to the CMB and

$$\begin{aligned} \mathbf{p} &= \frac{\partial \left(r u_r \right)}{\partial r} \mathbf{e}_r \times \mathbf{B}_{\Sigma}, \\ \mathbf{s} &= \boldsymbol{\delta}_{\Sigma} \times B_r \mathbf{e}_r, \qquad \text{with} \quad \boldsymbol{\delta}_{\Sigma} = r \frac{\partial \mathbf{u}_{\Sigma}}{\partial r}, \\ \mathbf{t} &= \left(\mathbf{u}_{\Sigma} \times \frac{\partial \left(r B_r \right)}{\partial r} \mathbf{e}_r \right), \end{aligned} \tag{39}$$

where $\boldsymbol{\delta}_{\Sigma}$ has the dimension of a velocity. Finally, we write the condition of no toroidal field induction as

$$\forall l \geq 1, \forall m \in [0, l], \quad \sqrt{2l(l+1)} v_l^{0,m} = (p_l^{+,m} + s_l^{+,m} + t_l^{+,m} + p_l^{-,m} + s_l^{-,m} + t_l^{-,m}). \tag{40}$$

This equation is satisfied for negative m if it is satisfied for positive m. Equation (40) for $(m = 0)$ involves only real quantities. The third term $\mathbf{t}$ can be evaluated in the same way as $\mathbf{v}$ above (see (35)) except that B_r is to be replaced by $\partial(rB_r)/\partial r$. The first term can be treated in an analogous manner using

$$\frac{\partial(ru_r)}{\partial r} = \frac{1}{r}\frac{\partial(r^2u_r)}{\partial r} = -\boldsymbol{\nabla}_1 \cdot \mathbf{u}_\Sigma \tag{41}$$

(since $u_r = 0$ at the boundary). Finally, there remains to calculate the quantities s^+ and s^- for the second term $\mathbf{s}$. They can be obtained from the components δ^+ and δ^- of $\boldsymbol{\delta}_\Sigma$,

$$\boldsymbol{\delta}_\Sigma = \delta^+\mathbf{e}_+ + \delta^-\mathbf{e}_-, \tag{42}$$

through

$$s^\pm = \pm \mathrm{i}B_r\delta^\pm. \tag{43}$$

The condition of no toroidal field induction gives us a first relationship between the vector spherical harmonic expansions of the flow and its radial derivative.

The condition (16) on the poloidal part of the induction equation gives

$$\forall\, l \geq 1, \forall m \in [0, l], \qquad \frac{\partial}{\partial r}\left(r(v_l^{+,m} - v_l^{-,m})\right) = -l\left(v_l^{+,m} - v_l^{-,m}\right). \tag{44}$$

and then

$$\forall l \geq 1, \forall m \in [0, l], \quad p_l^{+,m} + s_l^{+,m} + t_l^{+,m} - p_l^{-,m} - s_l^{-,m} - t_l^{-,m} = -l\left(v_l^{+,m} - v_l^{-,m}\right). \tag{45}$$

These relations hold for negative m if they hold for positive m. For $m > 0$, s^+ and s^- can be determined independently from the components of $\mathbf{v}$ by adding and subtracting equations (40) and (45). The $m < 0$ coefficients of s^+ and s^- are immediately obtained from the $m > 0$ coefficients of s^- and s^+ respectively (see (33)). For $m = 0$, $s_l^{-,0} = (s_l^{+,0})^\dagger$. As a matter of fact, equation (40) gives the real part of $s_l^{+,0}$ while equation (45) gives its imaginary part. The final step consists in calculating separately δ^+ and δ^- from s^+ and s^- using (43). In summary, the two conditions on toroidal and poloidal SV need to be considered together and give a relationship between $\mathbf{u}$ and its radial derivative.

In the presence of a conducting layer at the bottom of the mantle, equation (40) is modified as

$$\sqrt{2l(l+1)}v_l^{0,m} = (p_l^{+,m} + s_l^{+,m} + t_l^{+,m} + p_l^{-,m} + s_l^{-,m} + t_l^{-,m}) - \tau_G \frac{\partial}{\partial t}\left(v_l^{+,m} + v_l^{-,m}\right), \quad (46)$$

and equation (45) as

$$p_l^{+,m} + s_l^{+,m} + t_l^{+,m} - p_l^{-,m} - s_l^{-,m} - t_l^{-,m} = -l\left(v_l^{+,m} - v_l^{-,m}\right) + \tau_G \frac{\partial}{\partial t}\left(v_l^{+,m} - v_l^{-,m}\right). \quad (47)$$

3 MAGNETIC FIELD DATA

3.1 Dynamo simulations

We use geodynamo simulations, in an electrically conducting and rotating spherical fluid shell, to generate synthetic data and validate our methodology for estimating the shear. The simulations implement the equations of Boussinesq convection, thermochemical density anomaly transport, and magnetic induction in the MHD approximation.

First, we use the same series of simulations as Aubert and Finlay (2019), all calculated with a stress-free boundary condition at the CMB. For these simulations, the core surface flow can unambiguously be defined as the flow at $r = r_C$. A distinguished limit (Dormy 2016), also known as path theory (Aubert et al. 2017), is employed to bridge the parameter space gap between the 'Coupled Earth model' by Aubert et al. (2013) and the conditions of the Earth's core by relating the parameters of the simulation to a single variable ϵ. The four dimensionless numbers of the simulations are the flux-based Rayleigh, Ekman, Prandtl, and magnetic Prandtl numbers

$$\begin{aligned} Ra_F &= \frac{gF}{4\pi\rho\Omega^3 D^4} = \epsilon Ra_F(CE), \quad E = \frac{\nu}{\Omega D^2} = \epsilon E(CE), \quad Pr = \frac{\nu}{\kappa} = 1, \\ P_m &= \frac{\nu}{\eta} = \sqrt{\epsilon} P_m(CE), \end{aligned} \quad (48)$$

where $D = r_C - r_I$, r_I, g, Ω, ρ, ν, κ, and η are, respectively, the fluid shell depth, the inner core radius, the gravity at radius r_C, the rotation rate, the fluid density, viscosity, thermochemical and magnetic diffusivities. Here, $Ra_F(CE) = 2.7 \times 10^{-5}$, $E(CE) = 3 \times 10^{-5}$, $P_m(CE) = 2.5$ are the control parameters of the Coupled Earth dynamo model. The scaling factor ϵ ranges from $\epsilon = 1$ to $\epsilon = 10^{-7}$. The two end-points describe respectively so named *0p* dynamo (the Coupled Earth model) and *100p* dynamo, hopefully, representative of the Earth's core conditions. Here, synthetic

Table 1. Summary of the main characteristics for the dynamo considered to build the prior covariance matrices. N^* is the number of snapshots considered for constructing the prior matrices. ΔT^* is the time span covered by the dynamo free run. The Ekman (E), magnetic Prandtl (P_m), magnetic Reynolds (R_m) numbers and the turn-over (τ_U) and Alfvén (τ_A) timescales are defined in the text.

dynamo	ΔT^* (yr)	N^*	E	P_m	R_m	τ_U (yr)	τ_A (yr)
Op	67 050	746	3×10^{-5}	2.5	942	140	100
50p	20 000	1000	10^{-8}	0.045	1082	125	14

data are generated from the *0p* and from the *50p* simulations for which $\epsilon = 1$ and 3.33×10^{-4} (Aubert and Finlay 2019). The synthetic magnetic field models are truncated at degree 13, set by the cut-off between the core and crustal contributions in spatial spectra of geomagnetic field models (Langel and Estes 1982). We recall in Table 1 the main characteristics of the dynamo simulations used to build the prior information when inverting for the flow and/or the shear at the top of the core (see §4).

Because we are interested in the recovery of the core flow and shear from geomagnetic data, we scale time from numerical to geophysical units based on the turn-over time, following Lhuillier et al. (2011). The magnetic field Gauss coefficients are first scaled so as to fit for harmonic degrees $2 \leq l \leq 13$ the numerical spatial spectrum

$$S_{MF}(l) = (l+1) \sum_{m=0}^{l} g_l^{m2} + h_l^{m2} \tag{49}$$

averaged over the dynamo time-span, to the spectrum of a geomagnetic field model (the CHAOS-6 model of Finlay et al. 2016). Then the numerical time is scaled by fitting for $l \in [2-13]$ the SV time scale

$$\tau_{SV}(l) = \sqrt{\frac{S_{MF}(l)}{S_{SV}(l)}} \tag{50}$$

obtained for the dynamo to $415/l$ (in years), where a definition similar to (49) is used for the SV spatial spectrum $S_{SV}(l)$.

Following Glatzmaier and Roberts (1996), the model includes a thin electrically conducting layer above the CMB to provide magnetic coupling between the core and the mantle. Modification of the boundary conditions arising from this conducting layer is taken into account for the toroidal

components, but not for the poloidal ones (see Appendix B for the expression of these conditions). The layer conductivity σ_m and thickness δ_m enter the dimensionless number

$$\Sigma = \frac{\sigma_m \delta_m}{\sigma_c D}\,, \tag{51}$$

ratio of the mantle and core conductances, with σ_c the conductivity of the fluid core. Σ is taken as 10^{-4} in the path simulations. We have

$$\tau_G = \frac{r_C}{D}\Sigma R_m \tau_U\,, \tag{52}$$

where $R_m = UD/\eta$ is the magnetic Reynolds number and $\tau_U = D/U$ the turn-over time-scale, with U the r.m.s velocity over the fluid core. The path simulations preserve R_m to values about 1000 and τ_U to values around 130 yr (see Table 1) so that $\tau_G \approx 20$ yr whatever the value of ϵ along the path. As a result, considering $|B_r|(r = r_C)/|B| \sim 1/8$ for Earth-like geodynamo simulations (Aubert et al. 2009, with $|B|$ the r.m.s. magnetic field inside the fluid core) and the values for the Alfvén time $\tau_A = D\sqrt{\rho\mu}/|B|$ found for the path simulations (Aubert et al. 2017, with μ the magnetic permeability), we can rewrite the dimensionless mantle conductance as $Q = \frac{\tau_G}{\tau_A}\frac{B_r}{|B|}\frac{D}{r_C}$ – see §2.2 for the definition of Q. We obtain $Q \sim 2 \times 10^{-2}$ and $Q \sim 10^{-1}$ for the *0p* and *50p* simulations respectively. These low values, together with the condition $\tau_G \ll \tau_U$, justify treating the mantle as insulating when considering decadal flow changes in the path simulations.

We also use for validating our approach magnetic data extracted from a simulation calculated with a no-slip boundary condition at the CMB and an insulating mantle, the *S1* numerical dynamo of Schaeffer et al. (2017). It has been obtained for $E = 10^{-6}$, $Pr = 1$, and $P_m = 0.2$. The magnetic Reynolds number has been estimated as $R_m = 546$. Similarly to the path dynamos of Aubert et al. (2017), the simulation *S1* is part of a series, which approximately preserves R_m and super criticality Ra/Ra_c (Ra_c Rayleigh number for the onset of thermal convection).

3.2 Geomagnetic field models

We consider as geomagnetic data the COV-OBS-x2 field model that covers the period 1840-2020 (Huder et al. 2020). The COV-OBS-x2 model results from a spatio-temporal regression of magnetic records from land surveys, ground-based observatories, and satellite missions. The model

is expanded up to spherical harmonic degree 14. Its coefficients are provided in time using order 4 cubic splines with knots every two years. The model is constructed within a stochastic framework, where a priori temporal correlations are derived from auto-regressive processes of order 2, as suggested by the temporal spectrum of observed field series (Gillet et al. 2013). This Bayesian approach allows the proposal of a model expectation (the most probable estimate) as well as of a posteriori model uncertainties. The former is considered below to build the observation and forward operators. The latter are used to build the SV data error covariance matrix. Here, we consider two snapshots for the years 2000 and 2018. This latter epoch is covered by Swarm data when the model reaches its highest accuracy. The comparison with the former epoch allows us to document the largest changes observed during the satellite era.

4 INVERSION METHODOLOGY

4.1 Solving for the core surface flow

We store the parameters describing the large-scale core surface flow ($u_l^{\pm m}$) in a vector $\mathbf{m}_u$. The flow model is expanded up to spherical harmonic degree L_u. We store the parameters describing the SV ($\partial_t U_{Bl}^m$) and the main field (U_{Bl}^m) respectively in vectors $\mathbf{y}_0$ and $\mathbf{g}$. These are expanded up to spherical harmonic degree 13. We then write the radial induction equation (36) in matrix form as

$$\mathbf{y}_0 = \mathsf{A}_0(\mathbf{g})\mathbf{m}_u + \mathbf{e}_0^r + \mathbf{e}_0^o = \mathbf{y}_0^u + \mathbf{e}_0^r + \mathbf{e}_0^o \,, \tag{53}$$

with $\mathbf{y}_0^u$ the SV prediction from the flow model $\mathbf{m}_u$. There are potentially two sources of errors associated with this equation: $\mathbf{e}_0^o$ stands for the observation errors on the SV field model coefficients, while errors of representativeness stored into $\mathbf{e}_0^r$ cover contributions from unmodelled processes, namely subgrid induction and diffusion (e.g., Eymin and Hulot 2005).

We wish to recover the flow by inverting Eq. (53). We assume that the statistics of the flow model and the errors are defined by their mean and cross-covariances. Under this Gaussian assumption, we face a linear inverse problem, for which we need to define the a priori cross-covariance matrix for the flow coefficients, $\mathsf{P}_u = \mathbb{E}\left(\mathbf{m}_u \mathbf{m}_u^T\right)$. In the following, the flow distri-

bution is supposed centered on zero, or $\mathbb{E}\left(\mathbf{m}_u\right) = \mathbf{0}$. This assumption is motivated by our poor knowledge of an appropriate background flow model in the geophysical case. We also need cross-covariance matrices for the two error terms in (53), namely $\mathsf{R}_0^o = \mathbb{E}\left(\mathbf{e}_0^o \mathbf{e}_0^{oT}\right)$ and $\mathsf{R}_0^r = \mathbb{E}\left(\mathbf{e}_0^r \mathbf{e}_0^{rT}\right)$. Both error sources are supposed independent the one from the other, or $\mathbb{E}\left(\mathbf{e}_0^r \mathbf{e}_0^{oT}\right) = 0$. The covariance matrix for the sum of the two errors is then $\mathsf{R}_0 = \mathsf{R}_0^r + \mathsf{R}_0^o$. We consider unbiased errors, so that $\mathbb{E}\left(\mathbf{e}_0^o\right) = \mathbb{E}\left(\mathbf{e}_0^r\right) = \mathbf{0}$. Finally, the solution to the linear inverse problem (53) is:

$$\hat{\mathbf{m}}_u = \left(\mathsf{A}_0^T \mathsf{R}_0^{-1} \mathsf{A}_0 + \mathsf{P}_u^{-1}\right)^{-1} \mathsf{A}_0^T \mathsf{R}_0^{-1} \mathbf{y}_0 \,. \tag{54}$$

Following Aubert (2013), we assume that numerical models of the Earth's dynamo simulate the state of the Earth's core well enough to provide the prior information needed to invert for core surface flow and shear. The cross-covariance matrices R_0^r and P_u are built from N^* samples of the fields $\mathbf{y}_0, \mathbf{g}$ and $\mathbf{m}_u$ from the dynamo simulations presented in § 3.1. First a crude empirical a priori covariance matrix for the flow is estimated from the samples as

$$\tilde{\mathsf{P}}_u = \frac{1}{N^* - 1} \sum_{k=1}^{N^*} \mathbf{m}_{u,k} {\mathbf{m}_{u,k}}^T \,. \tag{55}$$

However, this estimate is noisy because of the finite number of independent dynamo states. There are indications that this introduces spurious covariances (Sanchez et al. 2020; Schwaiger et al. 2023). In order to reduce their impact, while keeping the significant ones, we apply the "graphical LASSO" method (Friedman et al. 2007; Banerjee et al. 2008) on $\tilde{\mathsf{P}}_u$ and obtain P_u (see Appendix C). This method is known to reduce noise in empirical covariance matrix estimates. It also makes the covariance matrix less sensitive to the choice of samples. For the prior matrix considered here, this method allows conserving the strong cross-correlations between flow coefficients of the same order m and nearby degrees $l, l+1, l+2...$, due to the predominance of the geostrophic equilibrium in the dynamo simulation. These are common to other Earth-like dynamo simulations (e.g. Gillet et al. 2019).

Next, for each sample k we calculate the errors of representativeness as

$$\mathbf{e}_{0,k}^r = \mathbf{y}_{0,k} - \mathsf{A}_0\left(\mathbf{g}_k\right) \mathbf{m}_{u,k} \,. \tag{56}$$

The associated covariance matrix R_0^r is then obtained by applying the graphical LASSO to the

empirical estimate

$$\tilde{\mathsf{R}}_0^r = \frac{1}{N^* - 1} \sum_{k=1}^{N^*} \mathbf{e}_{0,k}^r \mathbf{e}_{0,k}^{r\,T} \,. \tag{57}$$

In the case of synthetic dynamo data, we consider no observation errors, so that $\mathsf{R}_0 = \mathsf{R}_0^r$. In the case of geophysical observations, the covariance matrix R_0^o is considered diagonal, and built from the dispersion within the ensemble of SV realizations of the COV-OBS-x2 model (see Section 3.2).

4.2 Solving for the radial shear in the flow at the top of the core

We now turn to the inversion of the shear at the top of the core, given an estimate of the surface flow. We store parameters describing the large scale component of $r\partial_r \mathbf{u}_\Sigma$ at the core surface (coefficients $\delta_l^{\pm m}$) in a vector $\mathbf{m}_\delta$. We write the two constraints from the horizontal component of the induction equation at the core surface (toroidal and poloidal) in matrix form, as

$$\mathbf{y}_t \equiv \mathsf{A}_t(\mathbf{g})\mathbf{m}_u = \quad \mathsf{B}_t(\mathbf{g})\mathbf{m}_\delta + \mathbf{e}_t^r \,, \tag{58}$$

$$\mathbf{y}_p \equiv \mathsf{A}_p(\mathbf{g})\mathbf{m}_u = \quad \mathsf{B}_p(\mathbf{g})\mathbf{m}_\delta + \mathbf{e}_p^r \,. \tag{59}$$

Vectors $\mathbf{e}_{t,p}^r$ stand for the errors of representativeness associated with those two constraints, here again, due to subgrid induction and diffusion. The two constraints shall be used simultaneously, and are concatenated as

$$\mathbf{y}_h \equiv \mathsf{A}_h(\mathbf{g})\mathbf{m}_u = \mathsf{B}_h(\mathbf{g})\mathbf{m}_\delta + \mathbf{e}_h^r = \mathbf{y}_h^\delta + \mathbf{e}_h^r \,, \tag{60}$$

with $\mathbf{y}_h^\delta$ the prediction to $\mathbf{y}_h$ from the model $\mathbf{m}_\delta$, $\mathsf{A}_h^T = \left[\mathsf{A}_t^T\ \mathsf{A}_p^T\right]$, $\mathsf{B}_h^T = \left[\mathsf{B}_t^T\ \mathsf{B}_p^T\right]$, and $\mathbf{e}_h^{r\,T} = \left[\mathbf{e}_t^{r\,T}\ \mathbf{e}_p^{r\,T}\right]$.

We note $\mathsf{P}_\delta = \mathbb{E}\left(\mathbf{m}_\delta \mathbf{m}_\delta^T\right)$ the a priori covariance matrix on $\boldsymbol{\delta}_\Sigma$ (supposed a priori of zero-mean). The cross-covariance matrix for the (supposed unbiased) errors of representativeness in Eq. (60) is noted $\mathsf{R}_h^r = \mathbb{E}\left(\mathbf{e}_h^r \mathbf{e}_h^{r\,T}\right)$. Inverting for $\mathbf{m}_\delta$ from 'observations' $\mathbf{y}_h$ comes down to a linear inference, whose solution is

$$\hat{\mathbf{m}}_\delta = \left(\mathsf{B}_h^T \mathsf{R}_h^{-1} \mathsf{B}_h + \mathsf{P}_\delta^{-1}\right)^{-1} \mathsf{B}_h^T \mathsf{R}_h^{-1} \mathbf{y}_h \,. \tag{61}$$

We investigate below the inversion for $\boldsymbol{\delta}_\Sigma$ assuming that we know the flow, in which case it is fair to ignore the propagation into Eq. (60) of the uncertainties on the flow inferred using Eq. (54).

It happens in practice that these latter "observation errors" would be, as for the core flow inverse problem, dominated by errors of representativeness.

As for the flow inversion, we build the prior cross-covariances on $\mathbf{m}_\delta$ from geodynamo samples. Dynamo simulations considered here have been computed under the stress-free boundary condition

$$\frac{\partial}{\partial r}\left(\frac{\mathbf{u}_\Sigma}{r}\right) = 0\,, \tag{62}$$

at $r = r_C$, so that

$$\boldsymbol{\delta}_\Sigma = r\frac{\partial \mathbf{u}_\Sigma}{\partial r} = \mathbf{u}_\Sigma, \tag{63}$$

or in matrix form $\mathbf{m}_\delta = \mathbf{m}_u$. As a consequence, one has $\mathsf{P}_\delta = \mathsf{P}_u$. From the geodynamo fields $\mathbf{g}, \mathbf{m}_u$ and $\mathbf{m}_\delta$ we calculate for all samples the errors of representativeness

$$\mathbf{e}^r_{h,k} = \mathsf{A}_h\left(\mathbf{g}_k\right)\mathbf{m}_{u,k} - \mathsf{B}_h\left(\mathbf{g}_k\right)\mathbf{m}_{\delta,k}\,. \tag{64}$$

Their associated covariance matrix R^r_h is then obtained by applying the graphical LASSO to the empirical estimate as

$$\tilde{\mathsf{R}}^r_h = \frac{1}{N^* - 1}\sum_{k=1}^{N^*} \mathbf{e}^r_{h,k}{\mathbf{e}^r_{h,k}}^T\,. \tag{65}$$

4.3 Diagnostics

Below we consider several diagnostics, whether it be in the domain of the observations or of the inverted model. We are in particular interested in the spatial spectra for $\mathbf{y}_h$, the quantities considered as observations when inverting for the shear, which we define as

$$S_h(l) = (l+1)\sum_{m=0}^{l} |{y_{t_l}}^m|^2 + |{y_{p_l}}^m|^2\,. \tag{66}$$

Furthermore, to measure how well the results of our inversions match the reference dynamo fields (shear or flow), we use a correlation coefficient, defined for two surface vector fields $\mathbf{a}(\theta,\phi)$ and $\mathbf{b}(\theta,\phi)$ as

$$c(\mathbf{a},\mathbf{b}) = \frac{\displaystyle\int_0^{2\pi}\int_0^{\pi} \mathbf{a}\cdot\mathbf{b}\sin\theta d\theta d\phi}{4\pi|\mathbf{a}||\mathbf{b}|}\,, \tag{67}$$

where

$$|\mathbf{a}|= \sqrt{\frac{1}{4\pi}\int_0^{2\pi}\int_0^{\pi}(a_\theta(\theta,\phi)^2 + a_\phi(\theta,\phi)^2)\sin\theta d\theta d\phi} \tag{68}$$

is the r.m.s. of the norm of the vector $\mathbf{a}$ over the CMB. We also evaluate the misfit between two vector fields as

$$m(\mathbf{a},\mathbf{b}) = \frac{|\mathbf{a}-\mathbf{b}|}{\sqrt{|\mathbf{a}||\mathbf{b}|}}\,. \tag{69}$$

A perfect recovery is characterized by a misfit of 0 and a correlation coefficient of 1.

Finally, we estimate the factor between the surface flow and the inverted surface shear $\boldsymbol{\delta}_\Sigma$ as α the coefficient that minimizes the functional

$$J_\delta(\alpha) = |\boldsymbol{\delta}_\Sigma - \alpha\mathbf{u}_\Sigma|\ . \tag{70}$$

When considering the shear inverted from the reference dynamo flow (resp. the inverted flow), $\mathbf{u}_\Sigma$ in (70) is the reference flow (resp. the inverted flow). When considering a set of K independent dynamo states, a set of functionals $\{J_\delta(\alpha,k)\}_{k\in[1,K]}$ is obtained from all the considered samples, and α is then the coefficient that minimizes $\tilde{J}_\delta(\alpha)$ the median over the samples of the $J_\delta(\alpha,k)$. Similarly, a scaling factor α between the reference dynamo flow and the inverted flow might be calculated from the functional

$$J_u(\alpha) = |\hat{\mathbf{u}}_\Sigma - \alpha\mathbf{u}_\Sigma|\ , \tag{71}$$

where here $\hat{\mathbf{u}}_\Sigma$ stands for the inverted flow.

5 RESULTS

We first present (§ 5.1) a validation of our methodology using data from stress-free geodynamo simulations, for which we expect $\boldsymbol{\delta}_\Sigma = \mathbf{u}_\Sigma$. We conduct both twin (§ 5.1.1) and sister experiments (§ 5.1.2). In the former case, the prior knowledge needed for the inverse problem (model and error cross-covariance matrices) and the synthetic observations are built from samples of a single simulation (namely *0p*). In the latter case, prior matrices are built from *0p* dynamo samples, while synthetic data are obtained from the more advanced *50p* dynamo. We then investigate a more realistic case where the surface shear is calculated from a flow estimated from the SV rather

than from the surface flow directly obtained from the simulation (§ 5.1.3). Next, we test in §5.2 our tools with data extracted from a dynamo calculated with the no-slip (instead of stress-free) boundary condition at $r = r_C$. We are thus getting closer to the geophysical configuration. Finally, we follow the same protocol with real data from the COV-OBS-x2 magnetic model (§ 5.3).

5.1 Flow shear from synthetic dynamo data: stress-free simulations

5.1.1 Twin experiments with stress-free synthetic data, knowing the large-scale flow

We first consider the case of twin experiments based on the *0p* simulation. Flow and shear are truncated at degree $L_u = 18$. This is slightly above the resolution limit lately considered for inverted core motions, thus mitigating aliasing issues (Gillet et al. 2019). For this first test, we assume that the surface flow $\mathbf{u}_\Sigma$ is exactly known up to degree L_u, and test our ability to recover the radial shear in the flow $\boldsymbol{\delta}_\Sigma$, from Eq. (61). This comes down to an ideal set-up, in order to verify that we are able to obtain information on $\boldsymbol{\delta}_\Sigma$. We refer to this case as T_u^a. We estimate $\boldsymbol{\delta}_\Sigma$ for 28 independent snapshots of the *0p* simulation and find that it is highly correlated with $\mathbf{u}_\Sigma$. We report the distribution of correlations and misfit values by providing the median together with the first and last quartile values (see Table 2, case T_u^a). The misfit values are nonetheless quite large (with a median of about 1.22) because the inverted $\boldsymbol{\delta}_\Sigma$ has a much simpler geometry than the surface flow. This is well illustrated in Fig. 1, which shows one representative example chosen in such a way that the correlation and misfit between $\mathbf{u}_\Sigma$ and $\boldsymbol{\delta}_\Sigma$ are close to their respective median values within all the considered snapshots. The two maps show the ϕ components of $\mathbf{u}_\Sigma$ and $\boldsymbol{\delta}_\Sigma$ superimposed with their associated streamlines. Although there is not a one-to-one correspondence between the estimated shear and the shear prescribed at the core surface by the boundary condition, the correlation between the two fields is striking and their amplitude is similar. Writing $\boldsymbol{\delta}_\Sigma = \alpha \mathbf{u}_\Sigma$, we find that the global misfit $J(\alpha)$ is minimized for $\alpha = 1.3$, close to the expected value of 1.

We also test to what extent this conclusion depends on the choice of the truncation degree L_h of poloidal and toroidal conditions (see eq. 60). We consider two values, $L_h = 18$ and $L_h = 13$, corresponding to the cases T_u^a and T_u^b. It turns out that the results of the two inversions are very similar, implying that the choice for the truncation level is not critical. For $L_h = 13$, the global

Table 2. Statistics for the surface shear estimation. Correlation c and misfit m between the estimated shear and the surface flow. Assuming proportionality between the flow and the shear, α indicates the coefficient that minimizes $J_\delta(\alpha)$. Cases labeled "T" and "S" denotes respectively for the twin and sister experiments. The subscript *u* points tests based on surface flows directly extracted from the simulations, in which case the diagnostics c and m are calculated with respect to the dynamo flow. In other cases, they are estimated from the inverted flow. Cases noted "$S1$" and "G" stand for investigations of synthetic data from the *S1* simulation and from geophysical data (for 2018) respectively. "prior" indicates the dynamo considered for building the various (prior and error) covariance matrices. "data" indicates the dynamo used to generate the synthetic data. "C" stands for *COV-OBS-x2* geomagnetic model. L_h is the truncation degree of $\mathbf{y}_h$. For synthetic experiments we provide values for the 25%, 50%, and 75% percentiles, with the correlation and misfit values written in that order: 25%:50%:75%.

case	prior	data	L_h	$c(\boldsymbol{u}_\Sigma, \boldsymbol{\delta}_\Sigma)$	$m(\boldsymbol{u}_\Sigma, \boldsymbol{\delta}_\Sigma)$	α
T_u^a	*0p*	*0p*	18	0.78 : 0.81 : 0.84	0.97 : 1.22 : 1.39	1.3
T_u^b	*0p*	*0p*	13	0.77 : 0.81 : 0.83	1.03 : 1.19 : 1.40	1.1
T	*0p*	*0p*	18	0.79 : 0.82 : 0.85	0.74 : 0.91 : 1.06	2.3
S_u	*0p*	*50p*	18	0.64 : 0.76 : 0.81	1.10 : 1.24 : 1.57	0.9
S	*0p*	*50p*	18	0.85 : 0.90 : 0.94	1.02 : 1.22 : 1.64	1.8
$S1^a$	*0p*	*S1*	18	0.71 : 0.77 : 0.82	0.74 : 1.01 : 1.26	0.8
$S1^b$	*50p*	*S1*	18	0.66 : 0.74 : 0.87	0.82 : 1.11 : 1.32	0.5
G	*50p*	*C*	18	0.97	3.76	4.3
G^Δ	*50p*	*C*	18	0.80	0.94	0.4

misfit $J(\alpha)$ is minimized when $\boldsymbol{\delta}_\Sigma = 1.1\mathbf{u}_\Sigma$, again close to the expected relationship $\boldsymbol{\delta}_\Sigma = \mathbf{u}_\Sigma$. The following results are obtained with $L_h = 18$.

5.1.2 Sister experiment with stress-free synthetic data, knowing the large-scale flow

We move further and add a new step in the estimation of $\boldsymbol{\delta}_\Sigma$, considering the sister experiment with *50p* as the reference, and *0p* for the prior. We refer to this case as S_u. Here, we estimate the surface shear for 40 independent snapshots. The correlation between estimated shear and surface flow remains high (see Table 2). From twin to sister experiments, the median value of the correlation has decreased from 0.81 to 0.76 while the misfit has slightly increased from 1.22 to 1.24. The misfit is minimized when $\alpha = 0.9$, which is close to the expected value of 1 as in the twin experiment.

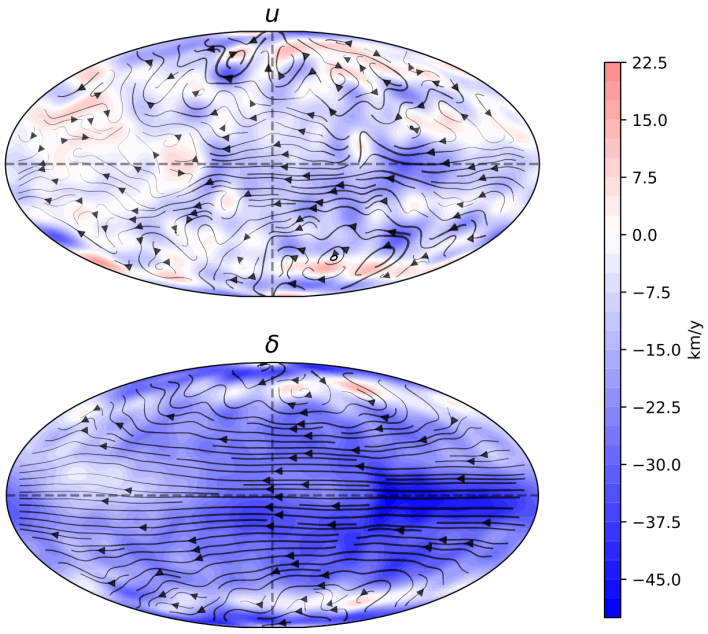

Figure 1. Comparison between the surface flow (top) and the inverted shear (bottom), in the case of twin experiments (case T_u^a), using the *0p* dynamo for both the data and the prior covariance matrices. The color scale gives the amplitude of the ϕ component.

Figure 2 (left) shows the comparison between surface flow and shear for a representative snapshot, which has a misfit m and a correlation c about the median value. The sister experiment, using the dynamo surface flow, validates the estimation of surface shear.

5.1.3 Experiments with stress-free synthetic data, and surface flow estimated from SV

We now infer $\mathbf{u}_\Sigma$ for independent snapshots of the magnetic field at the core surface and its SV. We build our prior covariance matrices from $0p$ simulations. The set-up for the flow inversion is very comparable to the one recently investigated by Schwaiger et al. (2023) when using dynamo priors. The only modification is the introduction of Graphical LASSO to build covariance matrices (see Appendix C). We shall consider successively twin (T) and sister (S) experiments. In the former case, we estimate 28 velocity snapshots from $0p$ simulation, and in the latter case, we estimate 40 snapshots from $50p$ simulation. Table 3 gives the statistics for the flow inversions. We find a high correlation between estimated and true surface flows. However, the estimated flow significantly underestimates the true flow by a factor of about 2.

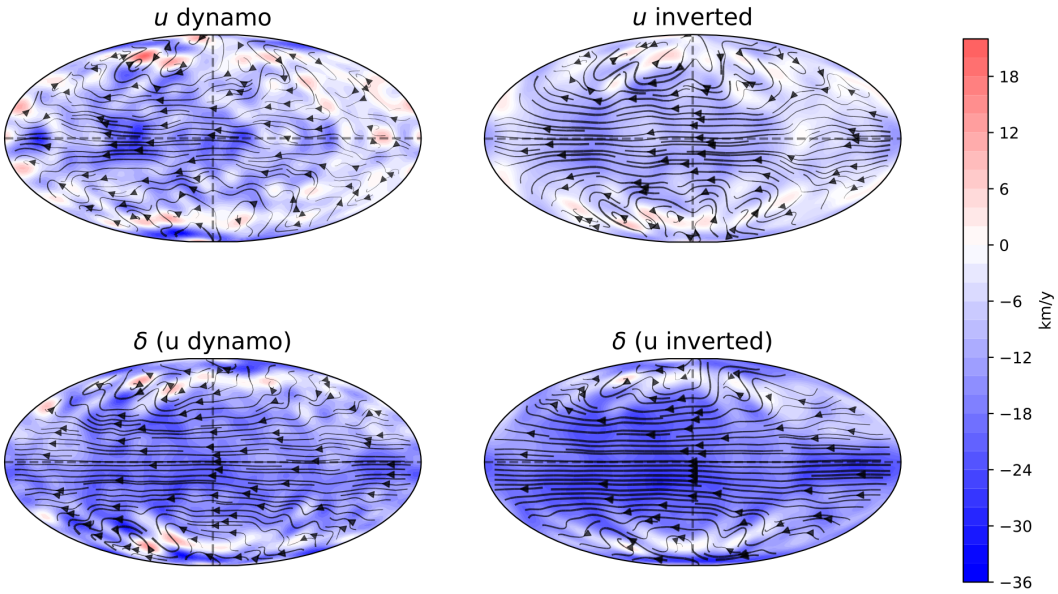

Figure 2. Comparison between flow (top) and shear (bottom) for sister experiments. The shear is calculated respectively from the dynamo flow (left, case S_u) and the inverted flow (right, case S). The color scale gives the amplitude of the ϕ component.

Then, we estimate shears from the inverted flows (case T and S, see Table 2). The correlation coefficients between inverted surface flow and shear maintain high values (median value 0.82 for T and 0.90 for S). Here, the misfits result from the large amplitude of the shear in comparison with the flow estimated from the SV. Figure 2 (right) shows maps for the SV inferred flow and the shear calculated with this flow for a representative example of the sister experiment S. This illustrates that the geometry of the shear and of the flow agrees quite well. However, we find a factor of about 2 between the surface shear and the inverted surface flow (namely 2.3 and 1.8 for T and S respectively). This disagrees with the expected relationship $\boldsymbol{\delta}_\Sigma = \mathbf{u}_\Sigma$. We have compared also the shears with the flows directly extracted from the dynamo simulations. Then, we approximately find $\boldsymbol{\delta}_\Sigma = \mathbf{u}_\Sigma$ (namely 1.1 and 0.9 for T and S respectively). We explain this discrepancy with the decisive role of the prior information in our shear estimation.

The impact of the prior information can be understood from the different spectra related to $\mathbf{y}_h$, the combined poloidal and toroidal constraints (see Fig. 3 bottom). We compare it with the spectra of the inverted flow (Fig. 3 top). In both cases, the power (of $\mathbf{y}_0$, the SV, and of $\mathbf{y}_h$)

Table 3. Statistics for surface flow estimations. Correlation c and misfit m between components of the estimated ($\hat{\mathbf{u}}_\Sigma$) and true ($\mathbf{u}_\Sigma$) surface flows. Assuming a linear relationship between the two flows, α indicates the coefficient that minimizes the functional $J_u(\alpha)$. Cases labeled "*T*" and "*S*" stand respectively for the twin and sister experiments. "prior" indicates the dynamo considered for building the various (prior and error) covariance matrices. "data" indicates the dynamo used to generate the synthetic data. We provide values for the 25%, 50%, and 75% percentiles, with the correlation and misfit values written in that order: 25%:50%:75%.

case	prior	data	$c(\hat{\mathbf{u}}_\Sigma, \mathbf{u}_\Sigma)$	$m(\hat{\mathbf{u}}_\Sigma, \mathbf{u}_\Sigma)$	α
T	*0p*	*0p*	0.79 : 0.82 : 0.85	0.74 : 0.91 : 1.06	0.5
S	*0p*	*50p*	0.66 : 0.77 : 0.81	0.8 : 0.89 : 1.29	0.4

increases with the spherical harmonic degree (see the blue lines in the two figures), and the errors of representativeness ($\mathbf{e}_0^r$ and $\mathbf{e}_h^r$ respectively, see the green dashed lines) explain a major part of the signal. However, we are in a much more favorable situation for the flow inversion than for the shear inversion. Indeed the terms involving the shear $\mathbf{y}_h^\delta$ (bottom figure) yield only a small contribution to $\mathbf{y}_h$, whereas the term involving the surface flows $\mathbf{y}_0^u$ (top figure) explains a major part of the radial SV (see the orange and dashed purple lines). As a result, our prior information on $\boldsymbol{\delta}_\Sigma$, taken as the same as the prior information on $\mathbf{u}_\Sigma$, plays a major role in our estimation of the shear amplitude. The expected amplitude of $\boldsymbol{\delta}_\Sigma$ thus matches the amplitude of the dynamo surface flow while the flow inverted from the radial SV has an amplitude that is only half the amplitude of the dynamo flow (in this example). This may explain why the estimation for $\boldsymbol{\delta}_\Sigma$ is too large compared with the inverted surface flow.

5.2 Flow shear from synthetic dynamo data: a no-slip simulation

We consider now SV data from the no-slip dynamo *S1* by Schaeffer et al. (2017), while we build the prior on the flow and the shear from the *0p* and the *50p* dynamos. Simulation *S1* has been obtained with a no-slip boundary condition at the top of the core, which does not prescribe a relationship between the radial shear in the flow and the surface flow in contrast with the stress-free boundary condition. The no-slip boundary condition is deemed appropriate to the geophysical case. Here, we aim to image the flow below the viscous (Ekman) boundary layer, much thicker

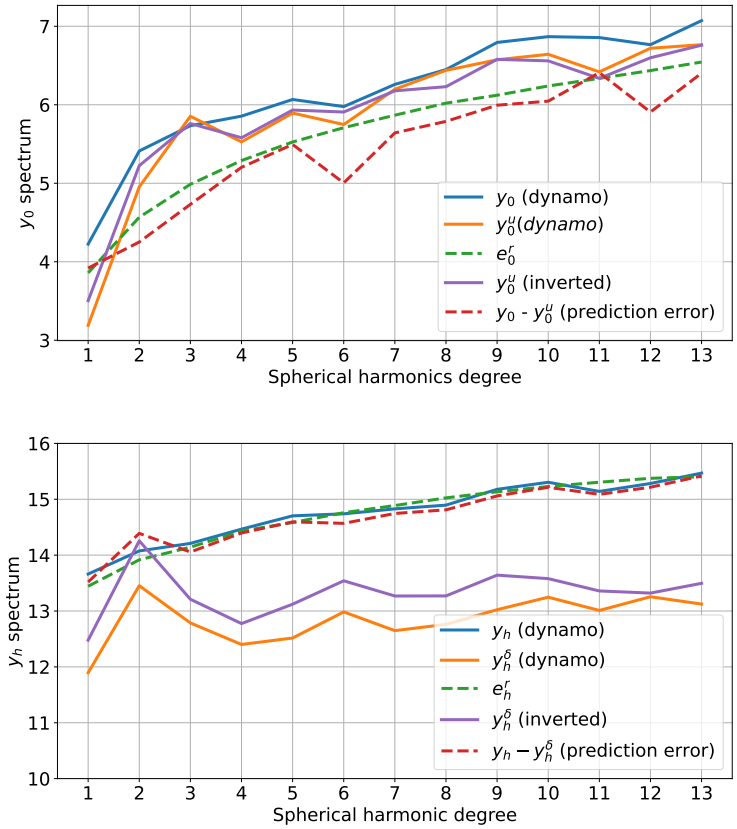

Figure 3. $\log_{10}$ of the energy spectra for the radial SV $\mathbf{y}_0$ (top, see Eq. 53) and the equation involving the radial shear in the flow $\mathbf{y}_h$ (bottom, see Eq. 60), in case S (sister experiment where the large-scale flow is inferred from radial SV, using *0p* data as prior matrices): observation (blue), a priori error (dashed green), reference field predictions (orange), model predictions (purple), prediction errors (dashed red). See Eq. (53) and (60) for the definitions of $\mathbf{y}_0^u$ and $\mathbf{y}_h^\delta$.

in the simulation than in the Earth's core, across which the magnetic field is supposed to be continuous. Since this location is not uniquely defined, we cannot define unambiguously the surface flow to compare with our flow estimation. Above all else, large variations with radius of $\boldsymbol{\delta}_\Sigma$ next to the core surface preclude any simple definition of the radial shear in the flow in no-slip dynamo simulations. Therefore, we shall only investigate whether the inverted surface flow and the inverted surface shear are similar. We estimate here the shear for 30 independent dynamo samples. We find again a strong correlation between surface flow and shear. The surface shear is only half the estimated flow when using the *50p* prior (to be compared with $\alpha \simeq 0.8$ for the inversion with the *0p* prior). Figure 4 (right) has been built for a representative example (where the misfit and the correlation are similar to their median values). We compare these maps for $\mathbf{u}_\Sigma$ and $\boldsymbol{\delta}_\Sigma$ with maps

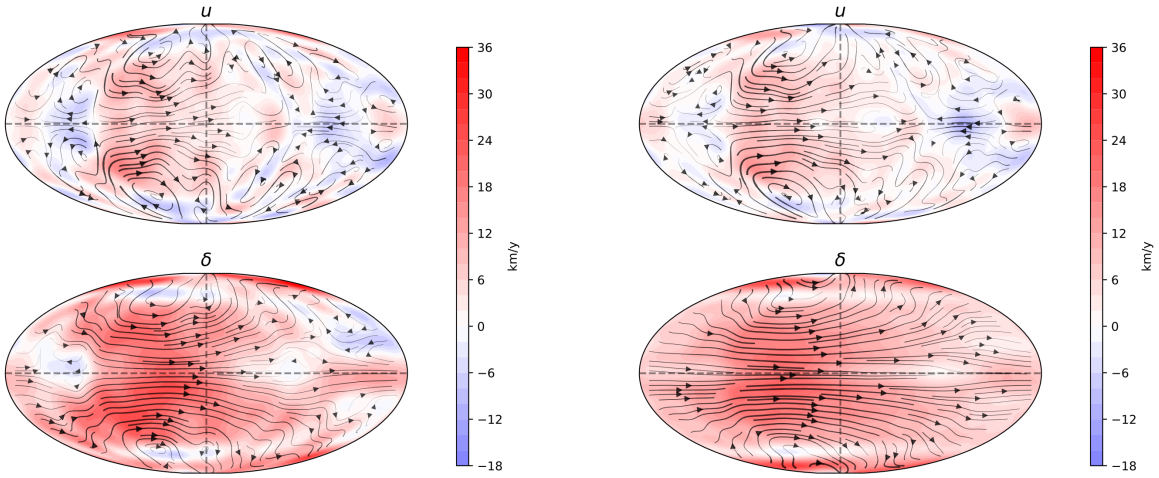

Figure 4. Comparison of inverted flow and shear from SV data of the *S1* no slip dynamo, using *0p* (left) and *50p* (right) to build the prior information (cases $S1^{a,b}$).

obtained for the same snapshot but with prior information given by the *0p* dynamo (left). We see again that the prior information is much more important for $\boldsymbol{\delta}_\Sigma$ than for $\mathbf{u}_\Sigma$. Figure 4 shows a nice agreement between the two quantities. We build on this result to consider geomagnetic data.

5.3 Flow shear at the core surface: application to geomagnetic data

We consider here the main field and SV Gauss coefficients from the COV-OBS-x2 geomagnetic field model for the epochs 2000 and 2018 (Huder et al. 2020). We conduct exactly the same suite of calculations as for the *S1* synthetic data above. We employ again the *50p* simulation for building the prior information. Using surface flow models obtained by inverting the radial induction equation, we solve the inverse problem for $\boldsymbol{\delta}_\Sigma$. Figure 5 presents a comparison between the maps of $\boldsymbol{\delta}_\Sigma$ and of $\mathbf{u}_\Sigma$. We recover the expected equatorial symmetry. Overall, the two vector fields have similar directions. Both the flow and the shear show a smooth structure, with less medium scales than the quantities estimated from *S1* synthetic data. They display the features present in estimations of core surface flows for the recent epochs and are dominated by westward surface flows/shears at low latitudes in a hemisphere centered on the Greenwich meridian. We find also emergence of Eastward flow under the Pacific Ocean from 2000 to 2018, as already reported by Finlay et al. (2023). There is a high correlation between flow and shear. We estimate

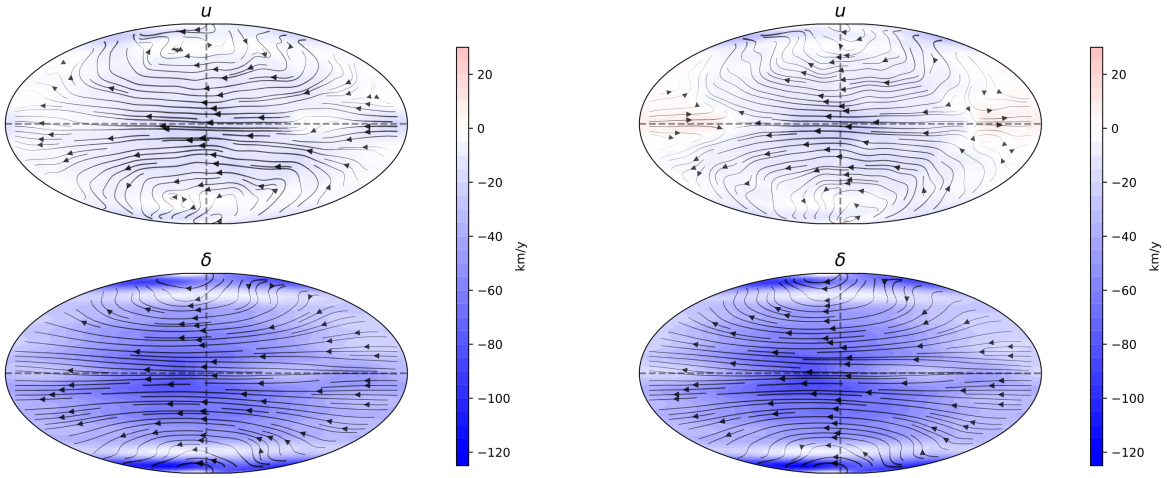

Figure 5. Comparison of the flow (top) and shear (bottom) inverted from the COV-OBS-x2 model, using *50p* as the prior and a truncation degree $L_h = 18$, at epoch 2000 (left) and 2018 (right).

$\boldsymbol{\delta}_\Sigma \sim 4.3\,\mathbf{u}_\Sigma$ for the year 2018 and *50p* prior ($\boldsymbol{\delta}_\Sigma \sim 4.7\,\mathbf{u}_\Sigma$ with the *0p* prior). Similarly to the example illustrating estimations from *S1* synthetic data with the same prior (see Fig. 4 right), the surface shear only partially reproduces spatial changes in the flow direction at the Equator. As shown in Fig. 6, a large correlation is also found between the flow increment $\Delta\mathbf{u}_\Sigma = \mathbf{u}_\Sigma(t = 2018) - \mathbf{u}_\Sigma(t = 2000)$ and the shear increment $\Delta\boldsymbol{\delta}_\Sigma = \boldsymbol{\delta}_\Sigma(t = 2018) - \boldsymbol{\delta}_\Sigma(t = 2000)$ – see the case G^Δ in Table 2. Here, we find $\Delta\boldsymbol{\delta}_\Sigma \sim 0.4\Delta\mathbf{u}_\Sigma$ when using the *50p* prior (and $\Delta\boldsymbol{\delta}_\Sigma \sim 0.6\Delta\mathbf{u}_\Sigma$ using the *0p* prior). The relationship between the shear and the flow thus seems to depend on the frequency.

Our analysis of geophysical data is at odds with the tests performed from synthetic data, as the surface flow and shear do not have similar amplitudes but rather the shear is much stronger. This questions the prior information used to calculate the surface shear. One possible explanation is the non-negligible role of mantle electrical conductivity. We need numerical simulations calculated with several values of mantle conductance to go further.

6 DISCUSSION

All our tests yield a clear correlation between the flow and the radial shear in the flow at the core surface. The results for the *0p* and *50p* path dynamos are consistent with the relationship

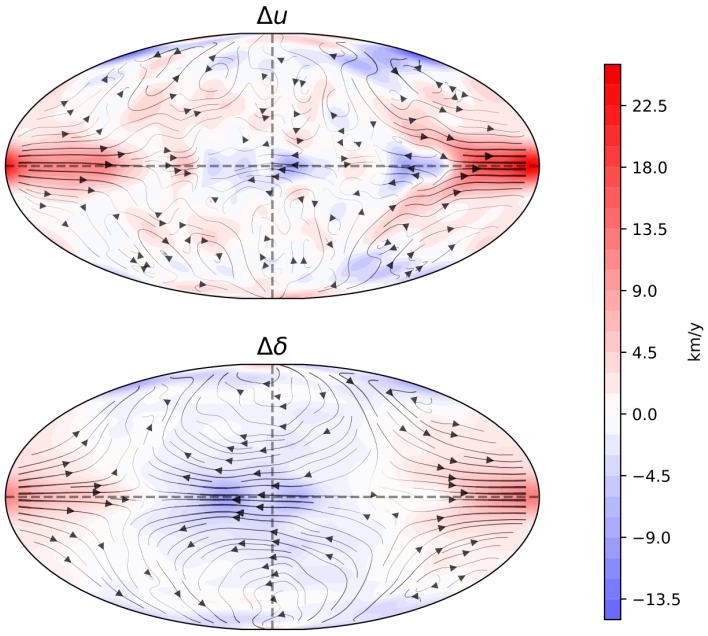

Figure 6. Flow increment (top) and shear increment (bottom) between epochs 2000 and 2018, as inverted from the COV-OBS-x2 model, using the *50p* prior.

$\boldsymbol{\delta}_\Sigma = \mathbf{u}_\Sigma$ as anticipated for dynamo models with stress-free boundary conditions. Less expectedly, this conclusion also holds for tests with synthetic data obtained from the *S1* model, calculated with no-slip boundary conditions. We find that unfortunately, the value of the ratio between flow and shear varies with the dynamo model used to build the necessary prior information. This makes it more difficult to reach firm conclusions when applying the method to actual data.

The surface shear that we infer from geomagnetic data for 2000 and 2018 also appears correlated with the surface flow. In contrast with synthetic cases, the ratio between instantaneous maps of the flow and of the shear is much higher than 1, namely about 4. Correlation between flow and shear had been exhibited previously by Lloyd and Gubbins (1990) and Jackson and Bloxham (1991) for 1970. These studies differ from ours inasmuch as they treat the horizontal components of the SV as data, whereas we derive a condition to be satisfied by the flow and the shear that is independent of SV data. Also, Jackson and Bloxham (1991) used the poloidal part of the SV data only: this amounts to considering equation (45) but not (40). Jackson and Bloxham (1991) and Lloyd and Gubbins (1990) estimated the ratio between flow and shear to be about 2 and 6, respectively.

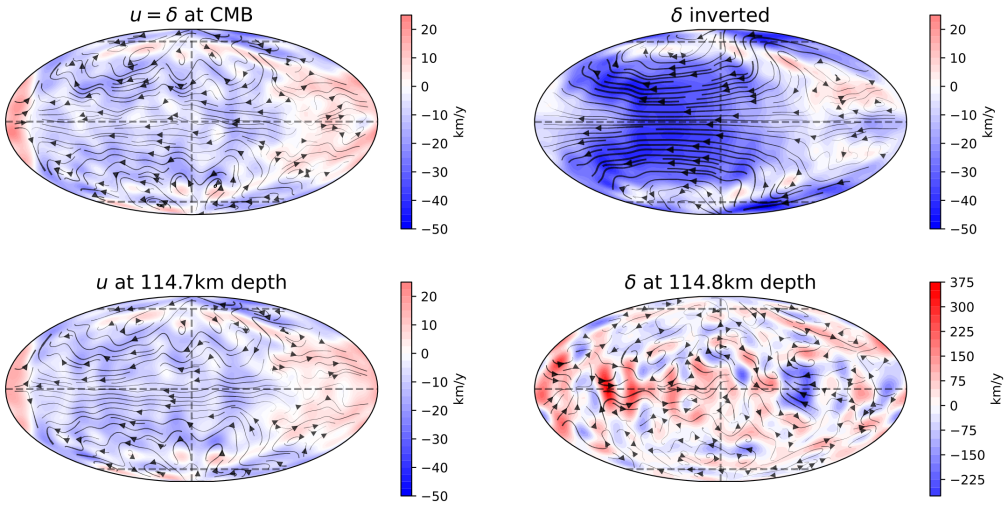

Figure 7. Shear in the flow at the Core surface (top left), shear in the flow inverted from the surface flow (top right), and shear in the flow (bottom left) and flow (bottom right) at about 6 Ekman depths δ_ν (or $r = 0.97 r_C$, with $\delta_\nu = r_C\sqrt{E}$), for one sample of the *0p* dynamo.

We find that the radial shear in the flow that we estimate from the induction equation at the CMB is unrelated to the shear at depth, for both stress-free (Fig. 7) and no-slip boundary (Fig. 8) conditions. The flow calculated at the surface and at depth are very similar in both cases. Here the fields are calculated from specific snapshots for which the flow components have been stored at all radii. The maps of the radial shear extracted from the geodynamo simulations at depth are the strongest in the equatorial region, and overall dominated by the azimuthal component. This intense shear arises because the flow, which is nearly QG, has small length scales in the cylindrical radial direction next to the equator. Conversely, these equatorial features are absent from the flow maps at the surface and at depth as well. This may explain why Amit et al. (2008) found a correlation between the flow and the radial shear in the flow at depth in their dynamo simulations ($E = 3 - 6 \times 10^{-4}$) only after down-playing the equatorial region.

Assuming a QG geometry for the flow (see ansatz (12c,d) of Labbé et al. (2015) and (2.1) of Bardsley (2018)), we can derive another expression relating the surface flow and its radial derivative at the CMB. When we undertook this study, we initially hoped to use this relationship together with conditions (15) and (16) to better constrain the surface flow. Unfortunately, we cannot combine the horizontal components of the induction equation at the core surface and the QG

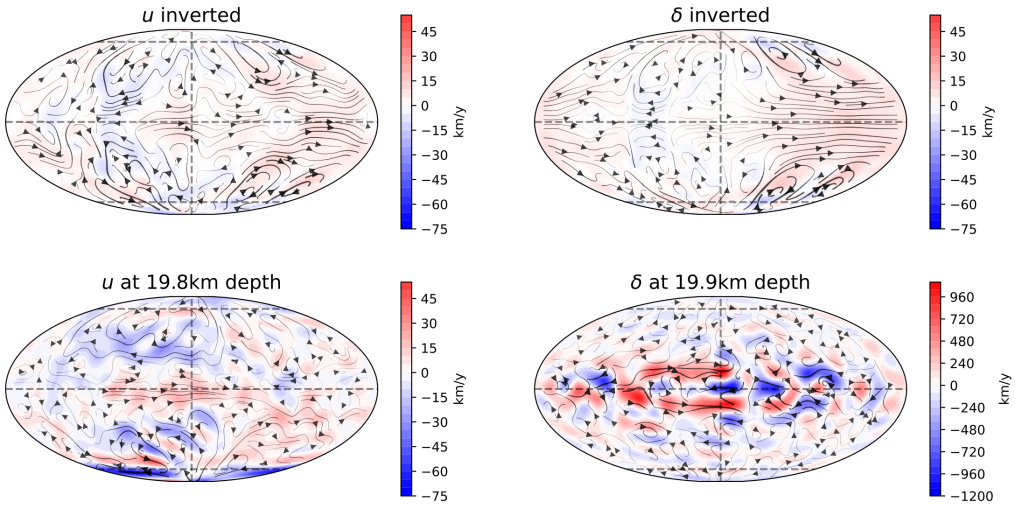

Figure 8. Surface flow estimated from radial SV (top left), shear in the flow inverted from the surface flow (top right), and shear in the flow (bottom left) and flow (bottom right) at about 6 Ekman depths ($r = 0.99 r_C$), for one sample of the *S1* dynamo.

approximation to better estimate the core surface flow because the QG ansatz and the continuity of $\partial \mathbf{B}/\partial t$ are not compatible at the CMB: the radial shear in the flow at the CMB is unrelated to the value predicted by the QG ansatz. Similarly, Jackson and Maffei (2020) needed the continuity of $\mathbf{B}$ at the CMB in a QG framework to calculate the boundary terms for the magnetic force in their plesio-geostrophic (PG) model. Our result thus casts doubt on the derivation of the surface terms in the PG model.

The surface shear would be a key ingredient of the dynamical equilibration in the presence of a conducting mantle. For Alfvén wave reflection on a conducting wall permeated by a uniform magnetic field, the appropriate boundary condition on the flow transforms from zero shear $\partial u/\partial n = 0$ (n indicating the direction normal to the boundary) to zero velocity $u = 0$ as the electrical conductivity of the wall increases from zero to infinity (see *e.g.* Schaeffer and Jault 2016). For a spherical boundary permeated by a laterally varying magnetic field, the situation is less simple but we expect similarly $\partial(\mathbf{u}/r)/\partial r$ to be weak if the mantle is electrically insulating and to become large compared to $\mathbf{u}/r^2$ with increasing conductivity of the mantle. The mention of Alfvén waves indicates that this description involves a discussion of force balance. As a matter of fact, the continuity of the horizontal components of the magnetic field $\mathbf{B}_\Sigma$ at the core-mantle interface

is equivalent to the equality of the Maxwell stress $B_r\mathbf{B}_\Sigma/\mu_0$ on either side of the CMB. Taking the radial component as invariant, the continuity of $\partial\mathbf{B}_\Sigma/\partial t$ thus amounts to the continuity of the components of the time derivative of the Maxwell stress parallel to the boundary. When the mantle is insulating, integrals of the Maxwell stress on the mantle side vanish, limiting the Maxwell stress on the core side. We explain this way our finding of weak shear in the *S1* dynamo even though it was not prescribed as a boundary condition. Conversely, in the presence of a conducting layer at the bottom of the mantle, Maxwell stresses on the mantle side have to be balanced by stresses on the core side. From the horizontal induction equation, we see that rapid time changes $\partial\mathbf{B}_\Sigma/\partial t$ arise from large surface shear. If the Earth's mantle had a strong conductance, an enhanced shear (from the term $\boldsymbol{\delta}_\Sigma \times B_r\mathbf{e}_r$) would be required to balance the term $\tau_G\partial\mathbf{v}^\pm/\partial t$ in equations (46) and (47):

$$s_l^{\pm,m} \sim \tau_G \frac{\partial}{\partial t} v_l^{\pm,m}, \quad \text{and as a result} \quad \delta_l^{\pm,m} \sim \tau_G \frac{\partial}{\partial t} u_l^{\pm,m} \tag{72}$$

(see equations (35) and (43)). In this situation, the surface shear would be well-constrained. On time scales for which the mantle is insulating (times large compared to τ_G) it will be difficult to ascertain the value of the shear. Alternatively, on short time scales for which the mantle conductivity is significant, we may hope to constrain the value of the shear at the core surface. This scenario now needs to be documented with dynamo models incorporating a conducting layer at the bottom of the mantle.

Our estimate of the surface shear, which is larger from geomagnetic data than from synthetic data, may be an indication of significant conductance of the lowermost mantle. Therefore, we may hope to constrain the mantle conductivity from an investigation of core dynamics. Holme et al. (2011) remarked that the observable SV varies on a time scale τ_{SA} that is independent of the harmonic degree and Christensen et al. (2012) found this statement to apply also to dynamo simulations. They argued that τ_{SA}, for $l \lesssim 10$, can primarily be interpreted as the time scale of the core surface flow changes. This observation has since been confirmed with dynamo simulations run at parameters closer to Earth's conditions (Aubert 2018).

The significance of the terms involving the mantle conductivity in the poloidal and toroidal conditions for the electrical field – see equations (46) and (47) – is thus measured by the ratio

606 τ_G/τ_{SA}. Taking τ_{SA} as 10 years, we find $\tau_G = \tau_{SA}$ for a mantle conductance about 7×10^7 S.
607 We may be able to gain insight into a conducting layer adjacent to the core from a detailed anal-
608 ysis of the time changes of the surface flow and shear if the mantle conductance is of this order
609 or larger. Within the framework we propose, the sensitivity of the core dynamics to the electrical
610 conductivity of the lower mantle is enhanced at short periods. Waves recently detected at interan-
611 nual periods from satellite data (Gillet et al. 2022) could thus be used as sources to shed light on
612 the conductance of the lowermost mantle adjoining the core.

613 ACKNOWLEDGMENTS

614 This work has been funded by the European Research Council (ERC) under the European Unions
615 Horizon 2020 research and innovation programme (GRACEFUL Synergy Grant agreement No
616 855677). It has also been partially supported by ESA in the framework of EO Science for Society,
617 through contract 4000127193/19/NL/IA (Swarm + 4D Deep Earth: Core). It has also been partially
618 French Space Agency (CNES) in the context of the Swarm mission.

619 AUTHORS CONTRIBUTION

620 The research program has been designed by DJ, NG, and MM. DJ derived the theoretical devel-
621 opments specific to this study. The numerical implementation and the production of the results
622 have been operated by IF, with some help from DJ and NG. NG, together with IF and DJ set up
623 the inverse problem. All three proposed most of the analysis of the results. New simulation data
624 have been produced by JA. The manuscript has been primarily written by DJ, NG, and IF, with
625 comments from MM and JA.

626 DATA AVAILABILITY

627 The core surface data of the analysed dynamo simulations are accessible at
628 https://gricad-gitlab.univ-grenoble-alpes.fr/Geodynamo/pygeodyn_data

The COV-OBS.x2 geomagnetic field model is available at

https://www.space.dtu.dk/english/research/scientific_data_and_models/magnetic_field_models

REFERENCES

H. Amit, J. Aubert, G. Hulot, and P. Olson. A simple model for mantle-driven flow at the top of Earth's core. *Earth Planets Space*, 60:845–854, 2008.

J. Aubert. Flow throughout the Earth's core inverted from geomagnetic observations and numerical dynamo models. *Geophys. J. Int.*, 192:537–556, 11 2013. doi: 10.1093/gji/ggs051.

J. Aubert. Geomagnetic acceleration and rapid hydromagnetic wave dynamics in advanced numerical simulations of the geodynamo. *Geophys. J. Int.*, 214:531–547, 2018.

J. Aubert and C. C. Finlay. Geomagnetic jerks and rapid hydromagnetic waves focusing at Earth's core surface. *Nature Geoscience*, 12(5):393–398, 2019.

J. Aubert, S. Labrosse, and C. Poitou. Modelling the palaeo-evolution of the geodynamo. *Geophys. J. Int.*, 179:1414–1428, 2009.

J. Aubert, C. C. Finlay, and A. Fournier. Bottom-up control of geomagnetic secular variation by the Earth's inner core. *Nature*, 502:219–223, 2013.

J. Aubert, T. Gastine, and A. Fournier. Spherical convective dynamos in the rapidly rotating asymptotic regime. *J. Fluid Mech.*, 813:558–593, 2017.

G. Backus, R. Parker, and C. Constable. *Foundations of geomagnetism*. Cambridge University Press, 1996.

G. E. Backus. Kinematics of geomagnetic secular variation in a perfectly conducting core. *Philosophical Transactions of the Royal Society of London. Series A, Mathematical and Physical Sciences*, 263:239–266, 1968.

O. Banerjee, L. El Ghaoui, and A. d'Aspremont. Model selection through sparse maximum likelihood estimation for multivariate gaussian or binary data. *J. Mach. Learn. Res.*, 9:485–516, 2008.

O. P. Bardsley. Could hydrodynamic Rossby waves explain the westward drift? *Proc. R. Soc. A*, 474 (2213):20180119, 2018.

J. Bärenzung, M. Holschneider, J. Wicht, S. Sanchez, and V. Lesur. Modeling and predicting the short-term evolution of the geomagnetic field. *J. Geophys. Res.: Solid Earth*, 123:4539–4560, 2018.

S. I. Braginsky. Torsional magnetohydrodynamic vibrations in the Earth's core and variations in day length. *Geomagnetism and aeronomy*, 10:1–8, 1970.

S. I. Braginsky. Short-period geomagnetic secular variation. *Geophys. Astrophys. Fluid Dyn.*, 30:1–78, 1984.

U. R. Christensen, I. Wardinski, and V. Lesur. Timescales of geomagnetic secular acceleration in satellite field models and geodynamo models. *Geophys. J. Int.*, 190:243–254, 2012.

E. Dormy. Strong-field spherical dynamos. *J. Fluid Mech.*, 789:500–513, 2016.

C. Eymin and G. Hulot. On core surface flows inferred from satellite magnetic data. *Phys. Earth Planet. Inter.*, 152:200–220, 2005.

C. C. Finlay, N. Olsen, S. Kotsiaros, N. Gillet, and L. Tøffner-Clausen. Recent geomagnetic secular variation from swarm and ground observatories as estimated in the CHAOS-6 geomagnetic field model. *Earth, Planets and Space*, 68:1–18, 2016.

C. C. Finlay, N. Gillet, J. Aubert, P. Livermore, and D. Jault. Gyres, jets and waves in Earth's core. *Nature Reviews Earth & Environment*, 4:377–392, 2023.

J. Friedman, T. Hastie, and R. Tibshirani. Sparse inverse covariance estimation with the graphical lasso. *Biostatistics*, 9:432–441, 2007. doi: 10.1093/biostatistics/kxm045.

F. Gerick, D. Jault, and J. Noir. Fast Quasi-Geostrophic Magneto-Coriolis Modes in the Earth's Core. *Geophys. Res. Lett.*, 48(4):e2020GL090803, 2021.

N. Gillet, D. Jault, C. C. Finlay, and N. Olsen. Stochastic modeling of the Earth's magnetic field: Inversion for covariances over the observatory era. *Geochemistry, Geophysics, Geosystems*, 14:766–786, 2013. doi: https://doi.org/10.1002/ggge.20041.

N. Gillet, L. Huder, and J. Aubert. A reduced stochastic model of core surface dynamics based on geodynamo simulations. *Geophys. J. Int.*, 219:522–539, 2019.

N. Gillet, F. Gerick, R. Angappan, and D. Jault. A dynamical prospective on interannual geomagnetic field changes. *Surveys in Geophysics*, 43:71–105, 2022.

G. A. Glatzmaier and P. H. Roberts. An anelastic evolutionary geodynamo simulation driven by compositional and thermal convection. *Physica D*, 97:81–94, 1996.

M. Greff-Lefftz and H. Legros. Core-mantle coupling and polar motion. *Phys. Earth Planet. Inter.*, 91: 273–283, 1995.

R. Hide and K. Stewartson. Hydromagnetic oscillations of the Earth's core. *Reviews of Geophysics and Space Physics*, 10:579–598, 1972.

R. Holme, N. Olsen, and F. L. Bairstow. Mapping geomagnetic secular variation at the core-mantle boundary. *Geophys. J. Int.*, 186:521–528, 2011.

L. Huder, N. Gillet, C. C. Finlay, M. D. Hammer, and H. Tchoungui. COV-OBS.x2: 180 years of geomagnetic field evolution from ground-based and satellite observations. *Earth, Planets and Space*, 72:160, 2020. doi: 10.1186/s40623-020-01194-2.

M. Istas, N. Gillet, C. Finlay, M. Hammer, and L. Huder. Transient core surface dynamics from ground and satellite geomagnetic data. *Geophys. J. Int.*, 233:1890–1915, 2023.

D. J. Ivers and C. G. Phillips. Scalar and vector spherical harmonic spectral equations of rotating magnetohydrodynamics. *Geophys. J. Int.*, 175:955–974, 2008.

A. Jackson and J. Bloxham. Mapping the fluid flow and shear near the core surface using the radial and horizontal components of the magnetic field. *Geophys. J. Int.*, 105:199–212, 1991.

A. Jackson and S. Maffei. Plesio-geostrophy for Earth's core: I. Basic equations, inertial modes and induction. *Proc. R. Soc. A*, 476(20200513), 2020.

D. Jault. Illuminating the electrical conductivity of the lowermost mantlle from below. *Geophys. J. Int.*, 202:482–496, 2015.

D. Jault and J.-L. Le Mouël. Physical properties at the top of the core and core surface motions. *Phys. Earth Planet. Inter.*, 68:76–84, 1991.

F. Labbé, D. Jault, and N. Gillet. On magnetostrophic inertia-less waves in quasi-geostrophic models of planetary cores. *Geophys. Astrophys. Fluid Dyn.*, 109:587–610, 2015.

R. Langel and R. Estes. A geomagnetic field spectrum. *Geophys. Res. Lett.*, 9:250–253, 1982.

F. Lhuillier, A. Fournier, G. Hulot, and J. Aubert. The geomagnetic secular-variation timescale in observations and numerical dynamo models. *Geophys. Res. lett.*, 38(L09306), 2011. doi: 10.1029/2011GL047356.

D. Lloyd and D. Gubbins. Toroidal fluid motion at the top of the Earth's core. *Geophys. J. Int.*, 100: 455–467, 1990.

D. E. Loper and E. R. Benton. On the spin-up of an electrically conducting fluid Part 2. Hydromagnetic spin-up between infinite flat insulating plates. *J. Fluid Mech.*, 43:785–799, 1970.

J. Luo, P. Marti, and A. Jackson. Waves in the Earth's core. II. Magneto-Coriolis modes. *Proc. R. Soc. A*, 478:20220108, 2022.

M. A. Pais and D. Jault. Quasi-geostrophic flows responsible for the secular variation of the Earth's magnetic field. *Geophys. J. Int.*, 173:421–443, 2008.

R. A. Phinney and R. Burridge. Representation of the elastic-gravitational excitation of a spherical Earth model by generalized spherical harmonics. *Geophys. J. R. astr. Soc.*, 34:451–487, 1973.

P. Roberts and S. Scott. On analysis of the secular variation 1. a hydrodynamic constraint: Theory. *J. Geomag. Geoelectr.*, 17:137–151, 1965.

P. H. Roberts and A. M. Soward. Magnetohydrodynamics of the Earth's core. *Annu. Rev. Fluid Mech.*, 4: 117–154, 1972.

S. Sanchez, J. Wicht, and J. Bärenzung. Predictions of the geomagnetic secular variation based on the ensemble sequential assimilation of geomagnetic field models by dynamo simulations. *Earth, Planets and Space*, 72:157, 2020. doi: https://doi.org/10.1186/s40623-020-01279-y.

N. Schaeffer and D. Jault. Electrical conductivity of the lowermost mantle explains absorption of core torsional waves at the equator. *Geophys. Res. Lett.*, 43:4922–4928, 2016.

730 N. Schaeffer, D. Jault, H.-C. Nataf, and A. Fournier. Turbulent geodynamo simulations: a leap towards
731 Earth's core. *Geophys. J. Int.*, 211:1–29, 2017.
732 N. Schnepf, A. Kuvshinov, and T. Sabaka. Can we probe the conductivity of the lithosphere and upper
733 mantle using satellite tidal magnetic fields? *Geophys. Res. Lett.*, 42, 2015. doi: 10.1002/2015GL063540.
734 T. Schwaiger, T. Gastine, and J. Aubert. Force balance in numerical geodynamo simulations: a systematic
735 study. *Geophys. J. Int.*, 219:S101–S114, 2019.
736 T. Schwaiger, D. Jault, N. Gillet, N. Schaeffer, and M. Mandea. Local estimation of quasi-geostrophic
737 flows in Earth's core. *Geophys. J. Int.*, 234:494–511, 2023. doi: https://doi.org/10.1093/gji/ggad089.
738 K. Stewartson. The dispersion of a current on the surface of a highly conducting fluid. *Mathematical*
739 *Proceedings of the Cambridge Philosophical Society*, 53:774–775, 1957.
740 K. Stewartson. On the motion of a non-conducting body through a perfectly conducting fluid. *J. Fluid*
741 *Mech.*, 8:82–96, 1960.

742 APPENDIX A: VECTOR SPHERICAL HARMONICS

743 We calculate the contravariant basis of the complex basis (27) as

$$\mathbf{e}^- = \frac{\mathbf{e}_+ \times \mathbf{e}_0}{J} = -\mathbf{e}_+ = (\mathbf{e}_-)^\dagger, \tag{A.1}$$

744 where J, the Jacobian of the basis $(\mathbf{e}_+, \mathbf{e}_0, \mathbf{e}_-)$, is $-\mathrm{i}$, and similarly

$$\mathbf{e}^+ = -\mathbf{e}_- = (\mathbf{e}_+)^\dagger, \qquad \mathbf{e}^0 = \mathbf{e}_0 = \mathbf{e}_r. \tag{A.2}$$

745 Therefore, the basis vectors are orthogonal and of unit norm

$$\mathbf{e}_+ \cdot \mathbf{e}_-^\dagger = 0, \qquad \mathbf{e}_+ \cdot \mathbf{e}_+^\dagger = 1. \tag{A.3}$$

746 The contravariant components of $\mathbf{v}$ in this basis are

$$v^\pm = \mathbf{v} \cdot \mathbf{e}^\pm = \mathbf{v} \cdot \mathbf{e}_\pm^\dagger = \frac{1}{\sqrt{2}} \left(\mp v^\theta + \mathrm{i} v^\phi \right), \quad v^0 = v^r. \tag{A.4}$$

747 Using the representation (10) of $\mathbf{v}$ to calculate v^θ and v^ϕ, we obtain

$$\begin{aligned} v^\pm &= \frac{1}{\sqrt{2}} \sum_{l=1}^{l=\infty} \sum_{m=-l}^{l} (\mp V_l^m + \mathrm{i} W_l^m) \left(\frac{\partial Y_l^m}{\partial \theta} \mp \frac{\mathrm{i}}{\sin\theta} \frac{\partial Y_l^m}{\partial \phi} \right) \\ &= \frac{1}{\sqrt{2}} \sum_{l=1}^{l=\infty} \sum_{m=-l}^{l} (\mp V_l^m + \mathrm{i} W_l^m) \left(\frac{\mathrm{d} P_l^m}{\mathrm{d}\theta} \pm \frac{m}{\sin\theta} P_l^m \right) \exp(\mathrm{i} m \phi) \end{aligned} \tag{A.5}$$

748 We have

$$\frac{\mathrm{d}}{\mathrm{d}\theta}\widehat{P}_l^m \pm \frac{m}{\sin\theta}\widehat{P}_l^m = \mp\sqrt{l(l+1)}\widehat{P}_l^{\pm,m} \tag{A.6}$$

749 (Phinney and Burridge 1973). Using (A.6), we transform (A.5) into

$$v^{\pm} = \mp\sum_{l=1}^{l=\infty}\sum_{m=-l}^{l}\frac{\sqrt{l(l+1)}}{\sqrt{2}}\left(\mp V_l^m + \mathrm{i}W_l^m\right)Y_l^{\pm,m} = \sum_{l=1}^{l=\infty}\sum_{m=-l}^{l} v_l^{\pm,m}Y_l^{\pm,m}, \tag{A.7}$$

750 with

$$\forall l \geq 1, -l \leq m \leq l, \quad v_l^{\pm,m} = \frac{\sqrt{l(l+1)}}{\sqrt{2}}\left(V_l^m \mp \mathrm{i}W_l^m\right). \tag{A.8}$$

751 APPENDIX B: BOUNDARY CONDITION ON THE MAGNETIC FIELD

We write the boundary conditions on the magnetic field at $r = c$ in the presence of an infinitely thin conducting layer. The radial component is continuous across the layer. We have at the core-mantle boundary

$$W_B = W_\delta, \tag{B.1}$$

and in the mantle conducting layer

$$\frac{\partial W_B}{\partial r} = -\frac{W_B}{\delta}. \tag{B.2}$$

Finally, the continuity of the components of the electrical field parallel to the boundary gives

$$\frac{1}{\mu\sigma_m\delta_m}W_\delta = -V - \frac{1}{\mu\sigma_c c}\frac{\partial(rW_B)}{\partial r}. \tag{B.3}$$

Similarly

$$V_B = V_\delta - \frac{\Phi}{c} \tag{B.4}$$

752 and

$$-\frac{V_\delta}{\mu\sigma_m\delta_m} = \frac{1}{\mu\sigma_c}\frac{1}{r}\left(\frac{\partial}{\partial r}(rV_B) - U_B\right) - W \tag{B.5}$$

$$-\frac{V_{\delta,l}^m}{\mu\sigma_m\delta_m} = \frac{1}{\mu\sigma_c}\frac{1}{r}\left(\frac{\partial}{\partial r}(rV_{B,l}^m) - U_{B,l}^m\right) + \frac{c}{l(l+1)}\frac{\partial U_{B,l}^m}{\partial t} \tag{B.6}$$

If we can neglect the diffusion term on the right-hand side, we obtain

$$V_{\delta,l}^m = \frac{\tau_G}{l(l+1)}\frac{\partial U_{B,l}^m}{\partial t} \tag{B.7}$$

Then, the boundary condition for the poloidal field becomes

$$V^m_{B,l} = \frac{1}{r}\frac{1}{l(l+1)}\frac{\partial}{\partial r}(r^2 U^m_{B,l}) = -\frac{U^m_{B,l}}{l+1} + \frac{\tau_G}{l(l+1)}\frac{\partial U^m_{B,l}}{\partial t}. \tag{B.8}$$

APPENDIX C: COVARIANCE MATRICES WITH GRAPHICAL LASSO

Empirical covariance matrices for the prior on the flow, the shear, and errors of representativeness have been obtained based on a finite set of samples from geodynamo simulations, using the Graphical LASSO (or 'G-LASSO', see Banerjee et al. 2008; Friedman et al. 2007) in order to reduce spurious cross-covariances. We recall here the main lines of this approach, in the case of the fluid flow a priori covariance matrix. From the rough estimate of Eq. (55), we first calculate the correlation matrix

$$\tilde{\mathsf{C}}_u = \mathsf{D}_u^{-1/2}\tilde{\mathsf{P}}_u\mathsf{D}_u^{-1/2}\,, \tag{C.1}$$

where D_u is the diagonal of the matrix $\tilde{\mathsf{P}}_u$. Following Istas et al. (2023), we then apply G-LASSO on $\tilde{\mathsf{C}}_u$. This algorithm provides a sparse estimate of the precision matrix Θ (inverse of the correlation matrix), by searching for

$$\hat{\Theta}(\lambda) = \mathrm{argmin}_{\Theta\geq 0}\left(\mathrm{tr}(\tilde{\mathsf{C}}_u\Theta) - \log\det(\Theta) + \lambda\sum_{j\neq k}|\Theta_{jk}|\right)\,, \tag{C.2}$$

where λ is an adjustable parameter. The output cross-covariance matrix is then

$$\mathsf{P}_u = \mathsf{D}_u^{1/2}\hat{\Theta}^{-1}\mathsf{D}_u^{1/2}\,. \tag{C.3}$$

Considering $\lambda = \infty$ sets off-diagonal elements of $\hat{\Theta}$ (and then of P_u) to zero, while for $\lambda = 0$ the method outputs $\mathsf{P}_u = \tilde{\mathsf{P}}_u$ (if inversible).

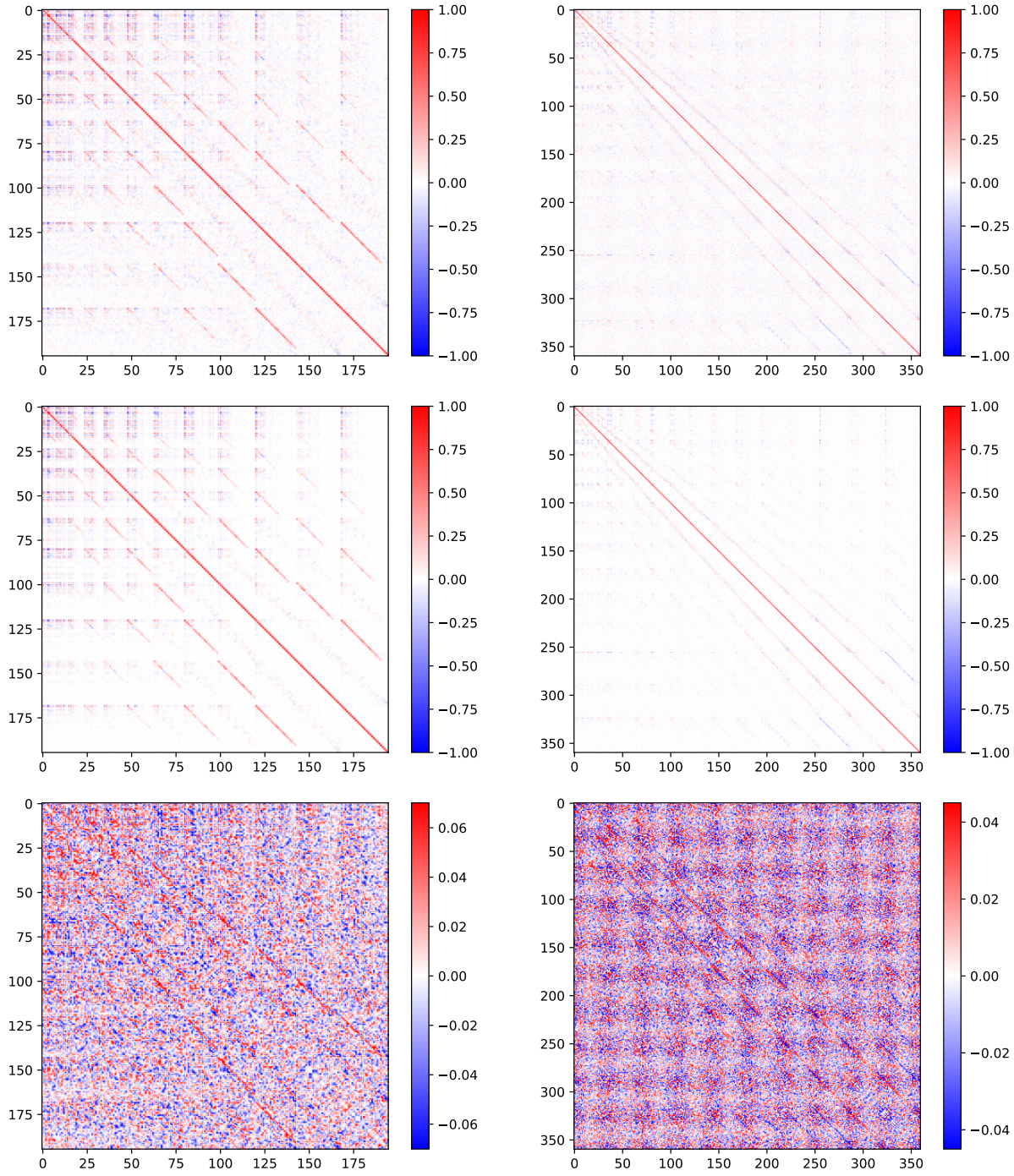

Figure A1. Left: correlation matrices for first 195 toroidal coefficients (i.e. up to harmonic degree $l = 13$) of the flow obtained for the *0p* dynamo: raw matrix $\tilde{\mathsf{C}}_u$ (top), C_u obtained after applying the G-LASSO with $\lambda = 0.07$ (middle), and the difference between the two (bottom). Coefficients are stored as follows: $t_1^{0,c}, t_1^{1,c}, t_1^{1,s}, t_2^{0,c}, t_1^{1,c}, t_2^{1,s}, t_2^{2,c}, t_2^{2,s}, t_3^{0,c}$... Right: same for the correlation matrix associated with $\tilde{\mathsf{R}}_h^r$ for the errors of representativeness, obtained after applying the G-LASSO with $\lambda = 0.05$.

Table A1. Correlation and misfits for the two horizontal components of the shear estimated from *50p* data, and using the *0p* prior, with and without application of G-LASSO to the prior matrices ($L_h = 18$).

case	$c(\mathbf{u}, \boldsymbol{\delta})$	$m(\mathbf{u}, \boldsymbol{\delta})$
with G-LASSO	0.64 : 0.76 : 0.81	1.10 : 1.24 : 1.57
without G-LASSO	0.56 : 0.70 : 0.75	1.82 : 2.13 : 2.59

We show in Fig. A1 (left) an example of the application of this algorithm for the matrix P_u. Our choice of $\lambda = 0.07$ is governed by the wish to keep as much as possible the off-diagonal strong correlations between coefficients of same order m but different degrees, while reducing spurious off-diagonal elements. This is illustrated by showing the difference between $\tilde{\mathsf{P}}_u$ and P_u. Similarly the cross-covariance matrix for the errors of representativeness R_h^r (resp. R_0^r) is obtained from $\tilde{\mathsf{R}}_h^r$ (resp. $\tilde{\mathsf{R}}_0^r$) when inverting for the shear (resp. the flow), as illustrated in Fig. A1 (right).

We provide in Table A1 the scores for the misfits and correlation coefficients when inverting for the shear in the case of twin and sister experiments. Using the G-LASSO significantly improves the scores in the latter case, justifying our preference this sparse estimate of the matrices.